Infrared Laser-Induced Grating Techniques for Diagnostics in Reactive Flows

Hot, Dina

2020

Document Version:
Publisher's PDF, also known as Version of record

Infrared laser-induced grating techniques for diagnostics in reactive flows

Dina Hot

LUND
UNIVERSITY

Akademisk avhandling som för avläggande av teknologie doktorsexamen vid tekniska fakulteten vid Lunds universitet kommer att offentligen försvaras fredagen den 15 maj 2020, kl. 9.15 i Rydbergssalen, Fysiska institutionen, Professorsgatan 1, Lund.

Fakultetsopponent: Prof. Dr. Thomas Dreier, Universität Duisburg-Essen, Tyskland

Academic thesis which, by due permission of the Faculty of Engineering at Lund University, will be publicly defended on Friday, 15th of May 2020, at 9.15 a.m. in the Rydberg hall at the Department of Physics, Professorsgatan 1, Lund, for the degree of Doctor of Philosophy in Engineering.

Faculty opponent: Prof. Dr. Thomas Dreier, University of Duisburg-Essen, Germany

Organization LUND UNIVERSITY Combustion Physics Department of Physics P.O. Box 118, SE-211 00 Lund, Sweden	**Document name** **DOCTORAL DISSERTATION** **Date of issue:** May 15, 2020 **CODEN:** LUTFD2/TFCP-225-SE
Author Dina Hot	Sponsoring organization

Title and subtitle

Infrared laser-induced grating techniques for diagnostics in reactive flows

Abstract

The work presented in this thesis is mainly focused on the development and application of infrared laser-induced grating techniques in order to measure the gas phase temperature and species concentrations in reactive flows. The two techniques used for this purpose are laser-induced grating spectroscopy (LIGS) and degenerate four-wave mixing (DFWM). Their coherent nature allows to perform laser-based diagnostics in the infrared spectral region where fundamental ro-vibrational transitions of several combustion-related molecular species can be utilized.

Gas phase temperature measurements has been performed with laser-induced thermal grating spectroscopy, known as LITGS. The single-shot precision and accuracy of mid-infrared LITGS was investigated in premixed CH_4/H_2/air flames at atmospheric pressure by probing the hot water absorption lines around 3.1 µm, resulting in a single-shot precision better than 1 % and an accuracy of 2.5 %. Furthermore, the technique has been applied in sooty premixed atmospheric C_2H_4/air flames. Besides the application of mid-IR LITGS, the alignment of the technique in terms of grating spacing, number of resolved oscillation peaks in the LITGS signal and its time characteristics has been investigated as well as misalignment effects. Attention has also been paid to select absorption lines which results in thermalization and hence are present in a LITGS excitation spectrum. In addition to LITGS, laser-induced electrostrictive grating spectroscopy (LIEGS) was investigated for possible application in harsh environments at temperatures up to 700 K. This study was carried out in the spectral band of oxygen at 760 nm and for two different geometrical alignments of LIEGS/LITGS.

Ammonia (NH_3) and hydrogen cyanide (HCN) are two molecular species of particular interest in the thermochemical conversion of biomass, which have fundamental or combinational vibrational bands in the mid-IR. Hence, species concentration measurements were carried out using mid-IR DFWM. A feasibility study has been performed for application of DFWM for ammonia detection around 2.3 µm. Moreover, DFWM was applied for HCN detection during the thermochemical conversion of straw pellets, where the HCN release history during the devolatilization stage was quantified at different flue gas temperatures.

Key words

Laser diagnostics, infrared, laser-induced grating spectroscopy, degenerate four-wave mixing, flames, temperature, concentration

Classification system and/or index terms (if any)

Supplementary bibliographical information		**Language** English
ISSN and key title 1102-8718		**ISBN** 978-91-7895-474-2 (print) 978-91-7895-475-9 (pdf)
Recipient's notes	**Number of pages** 174	Price
	Security classification	

Signature  Date: 2020-04-21

Infrared laser-induced grating techniques for diagnostics in reactive flows

Dina Hot

DOCTORAL THESIS

2020

LUND
UNIVERSITY

INFRARED LASER-INDUCED GRATING TECHNIQUES FOR DIAGNOSTICS IN REACTIVE FLOWS

Department of Physics
Faculty of Engineering
Lund University

Lund Reports on Combustion Physics, LRCP-225 (2020)
ISBN 978-91-7895-474-2 (print)
ISBN 978-91-7895-475-9 (pdf)
ISSN 1102-8718
ISRN LUTFD2/TFCP-225-SE

Printed in Sweden by Tryckeriet i E-huset
Lund 2020

Abstract

The work presented in this thesis is mainly focused on the development and application of infrared laser-induced grating techniques in order to measure the gas phase temperature and species concentrations in reactive flows. The two techniques used for this purpose are laser-induced grating spectroscopy (LIGS) and degenerate four-wave mixing (DFWM). Their coherent nature allows to perform laser-based diagnostics in the infrared spectral region where fundamental ro-vibrational transitions of several combustion-related molecular species can be utilized.

Gas phase temperature measurements has been performed with laser-induced thermal grating spectroscopy, known as LITGS. The single-shot precision and accuracy of mid-infrared LITGS was investigated in premixed CH_4/H_2/air flames at atmospheric pressure by probing the hot water absorption lines around 3.1 µm, resulting in a single-shot precision better than 1 % and an accuracy of 2.5 %. Furthermore, the technique has been applied in sooty premixed atmospheric C_2H_4/air flames. Besides the application of mid-IR LITGS, the alignment of the technique in terms of grating spacing, number of resolved oscillation peaks in the LITGS signal and its time characteristics has been investigated as well as misalignment effects. Attention has also been paid to select absorption lines which results in thermalization and hence are present in a LITGS excitation spectrum. In addition to LITGS, laser-induced electrostrictive grating spectroscopy (LIEGS) was investigated for possible application in harsh environments at temperatures up to 700 K. This study was carried out in the spectral band of oxygen at 760 nm and for two different geometrical alignments of LIEGS/LITGS.

Ammonia (NH_3) and hydrogen cyanide (HCN) are two molecular species of particular interest in the thermochemical conversion of biomass, which have fundamental or combinational vibrational bands in the mid-IR. Hence, species concentration measurements were carried out using mid-IR DFWM. A feasibility study has been performed for application of DFWM for ammonia detection around 2.3 µm. Moreover, DFWM was applied for HCN detection during the thermochemical conversion of straw pellets, where the HCN release history during the devolatilization stage was quantified at different flue gas temperatures.

Populärvetenskaplig sammanfattning

En stor del av världens energikällor är baserade på förbränning och kan återfinnas i allt från bilar och båtar som drivs av förbränningsmotorer till gasturbiner och kraftverk som används till elproduktion. Den centrala biten inom förbränning är en kemisk omvandling av bränslet då det reagerar med syre till att bilda de två huvudsakliga produkterna, vatten och koldioxid, samtidigt som en stor mängd värme produceras. Mycket av dagens fokus inom förbränningsforskningen handlar om att dels gradvis fasa ut användningen av fossila bränslen med alternativa bränslen så som biodiesel, alkoholer (ex. metanol och etanol), ammoniak, metaller och biomassa, och dels effektivisera den kemiska omvandlingen av befintliga bränslen ur ett hållbart miljömässigt perspektiv. Till det behövs en insikt i vad som sker under en förbränningsprocess.

Koldioxid är en växthusgas som sedan länge är förknippad med förbränning av kolväten, speciellt från fossila bränslen. Bortsett från koldioxid, bildas och släpps ut en mängd olika ämnen och föroreningar oavsett vilken typ av bränsle som förbränns. Att kunna mäta koncentrationen av dessa ämnen och även temperaturen vid olika tidpunkter under förbränningsprocessen, bidrar det till en ökad förståelse om hur förbränningen kan göras effektivare med mindre utsläpp.

I denna doktorsavhandling beskrivs utvecklingen och användningen av laserbaserade mätmetoder som fokuserar på att mäta de två ovannämnda parametrarna i flammor, nämligen koncentration och temperatur. Fördelen med laserbaserade mätmetoder framför mätprober och termoelement är att de möjliggör en beröringsfri mätmetod som inte påverkar flammans flöde, temperatur eller kemiska reaktioner. Många lasrar avger ljus i korta pulser som vanligtvis är några nanosekunder långa, vilket är en miljarddels sekund. Det innebär att en ögonblicksbild kan erhållas eftersom förbränningen inte ändras avsevärt under denna korta tid som det tar att utföra en mätning.

Det experimentella arbetet som presenteras i avhandlingen har fokuserats på användningen av så kallade icke-linjära optiska mättekniker där de baseras på växelverkan mellan tre laserstrålar och med det absorberande ämne som studeras. Dess fördel är att de kan vara väldigt känsliga då mycket små koncentrationer av ett ämne kan mätas och att signalen som bildas är en laserstråle som kan riktas bort från flamman innan den detekteras. Studierna har genomförts i den infraröda delen av spektrumet där många ämnen har en stark absorption. Några av dem är vätecyanid

och ammoniak som återfinns vid förbränning av biomassa. I arbetet presenteras temperaturmätningar utförda i flammor som baseras på vattenabsorption. Dessutom demonstreras en mätmetod som kvantifierar mängden vätecyanid som släpps ut vid förbränning av biomassa i form av pellets.

En bredare användning och en fortsatt vidareutveckling av laserbaserade mättekniker är en förutsättning för att fördjupa vår förståelse om vad som sker vid förbränning. Det är särskilt viktigt för kommande bränslen vars utsläpp ännu inte har studerats till fullo. Med erhållen kunskap genom mätningar finns det utsikter för att effektivisera motorer, gasturbiner och kraftverk, och även att minska utsläppen.

List of publications

The thesis is based on the following papers, which will be referenced by Roman numerals in the text. The papers are attached to the thesis in the listed order.

I. **Mid-infrared laser-induced thermal grating spectroscopy of hot water lines for flame thermometry**
D. Hot, A.L. Sahlberg, M. Aldén and Z.S. Li
Submitted to the 38th Proceedings of the Combustion Institute (2020)
Accepted for oral presentation at the 38th International Symposium on Combustion, Adelaide, Australia

II. **Mid-infrared laser-induced thermal grating spectroscopy in flames**
A.L. Sahlberg, D. Hot, J. Kiefer, M. Aldén and Z.S. Li
Proceedings of the Combustion Institute 36(3): 4515-4523 (2017)

III. **Misalignment effects in laser-induced grating experiments**
J. Kiefer, A.L. Sahlberg, D. Hot, M. Aldén and Z.S. Li
Applied Spectroscopy, 70, 2025-2028 (2016)

IV. **Investigation of laser-induced grating spectroscopy of O_2 for accurate temperature measurements in harsh environments**
D. Hot, A.L. Sahlberg, M. Aldén and Z.S. Li
Manuscript in preparation. (2020)

V. **Spatially and temporally resolved IR-DFWM measurement of HCN released from gasification of biomass pellets**
D. Hot, R. L. Pedersen, W. Weng, Y. Zhang, M. Aldén and Z.S. Li
Proceedings of Combustion Institute 37(2): 1337-1344 (2019)

VI. **Non-intrusive, in situ detection of ammonia in hot gas flows with mid-infrared degenerate four-wave mixing at 2.3 µm**
A.L. Sahlberg, D. Hot, M. Aldén and Z.S. Li
Journal of Raman Spectroscopy, 47(9):1140-1148 (2016)

Related work

Peer-reviewed publications not included in the thesis.

A. **Mid-infrared polarization spectroscopy measurements of species concentrations and temperature in a low pressure flame**
A.L. Sahlberg, D. Hot, R. L. Pedersen, J. Zhou, M. Aldén and Z.S. Li
Applied Spectroscopy, 73(6), 653-664 (2019)

B. **Comparison of an InSb detector and upconversion detector for infrared polarization spectroscopy**
R. L. Pedersen, D. Hot and Z.S. Li
Applied Spectroscopy, 72, 793-797 (2018)

C. **Instantaneous imaging of ozone in a gliding arc discharge using photofragmentation laser-induced fluorescence**
K. Larsson, D. Hot, J. Gao, C. Kong, Z.S. Li, M. Aldén, J. Bood and A. Ehn
Journal of Physics D: Applied Physics, 51, 135203 (2018)

D. **Quantitative imaging of ozone vapor using photofragmentation laser-induced fluorescence (LIF)**
K. Larsson, D. Hot, A. Ehn, A. Lantz, W. Weng, M. Aldén and J. Bood
Applied Spectroscopy, 71, 1578-1585 (2017)

The author's contributions

I. **Mid-infrared laser-induced thermal grating spectroscopy of hot water lines for flame thermometry**

D. Hot, A.L. Sahlberg, M. Aldén and Z.S. Li

Submitted to the 38th Proceedings of the Combustion Institute (2020)

This paper presents the single-shot precision and accuracy of mid-IR LITGS for flame thermometry when probing hot water lines around 3231 cm^{-1} in premixed laminar CH_4/H_2/air flames at atmospheric pressure.

I and Anna-Lena Sahlberg planned and performed the experiments. I did most of the data analysis and wrote the paper together with Anna-Lena Sahlberg, with help from Zhongshan Li and Marcus Aldén.

II. **Mid-infrared laser-induced thermal grating spectroscopy in flames**

A.L. Sahlberg, D. Hot, J. Kiefer, M. Aldén and Z.S. Li

Proceedings of the Combustion Institute 36(3): 4515-4523 (2017)

The first known application of mid-IR LITGS for temperature measurements in flames is demonstrated in this paper. The measurements were performed in premixed laminar C_2H_4/air flames when probing hot water lines around 3231 cm^{-1}.

I, Anna-Lena Sahlberg and Johannes Kiefer planned and performed the experiments. I took an active part in the discussions regarding the data analysis and interpretation of the results and wrote the paper together with the co-authors and with help from Zhongshan Li.

III. **Misalignment effects in laser-induced grating experiments**

J. Kiefer, A.L. Sahlberg, D. Hot, M. Aldén and Z.S. Li

Applied Spectroscopy, 70, 2025-2028 (2016)

This technical note discusses misalignment effects in laser-induced grating experiments which can be observed in the LIGS signals.

I, Anna-Lena Sahlberg and Johannes Kiefer planned and performed the experiments. Johannes Kiefer performed most of the data analysis and I

participated in the discussions regarding the interpretation of the results. Johannes Kiefer wrote the manuscript with input from all co-authors.

IV. **Investigation of laser-induced grating spectroscopy of O_2 for accurate temperature measurements in harsh environments**

D. Hot, A.L. Sahlberg, M. Aldén and Z.S. Li

Manuscript in preparation.

This manuscript deals with the investigation for practical applications of thermal and electrostrictive LIGS for temperature measurements when probing oxygen around 760 nm. The measurements were performed in heated air flows at 296-700 K using two different grating spacing alignments.

I planned and performed the experiments together with Anna-Lena Sahlberg. We did the data analysis and wrote the paper together, with help from Zhongshan Li.

V. **Spatially and temporally resolved IR-DFWM measurement of HCN released from gasification of biomass pellets**

D. Hot, R. L. Pedersen, W. Weng, Y. Zhang, M. Aldén and Z.S. Li

Proceedings of Combustion Institute 37(2): 1337-1344 (2019)

This work presents the first known attempt to quantify the HCN released from gasification of straw pellets during the devolatilization stage using mid-IR DFWM and the upconversion detector.

I had the responsibility for coordinating this work. I planned and performed the experiments together with Rasmus L. Pedersen, Wubin Weng and Yuhe Zhang. I took an active part in the discussions regarding the data analysis and I wrote the paper together with the co-authors and with help from Zhongshan Li and Marcus Aldén.

VI. **Non-intrusive, in situ detection of ammonia in hot gas flows with mid-infrared degenerate four-wave mixing at 2.3 µm**

A.L. Sahlberg, D. Hot, M. Aldén and Z.S. Li

Journal of Raman Spectroscopy, 47(9):1140-1148 (2016)

This paper presents the feasibility study of using mid-IR DFWM for ammonia detection in heated gas flows diluted with different buffer gases. The combination bands at 2.3 µm are targeted due to low spectral interference with water.

I took part in the planning of the measurements together with Anna-Lena Sahlberg and Zhongshan Li. I performed the experiments, did part of the data analysis and wrote the paper together with Anna-Lena Sahlberg, with help from Zhongshan Li.

Contents

1 Introduction

Combustion processes has been and will be the dominating source of energy in the foreseeable future. According to IEA[1] it constitutes 90 % of the global energy production, with biofuels and waste included. The increasing global warming and the negative health effects associated with pollutions as well as the limited resources of fossil fuels, motivates the current combustion research to make the processes more efficient and gradually phase out the use of fossil fuels with alternative fuels. This includes fuels such as biofuels, biomass, ammonia and metal fuel combustion. However, no matter what type of fuel it is, combustion is a complex process and an insight in the involved thermodynamics, fluid mechanics and chemistry is needed.

Laser-based diagnostics techniques play an important role in the combustion research since they can provide *in situ* non-intrusive information of the combustion process with high spatial and temporal resolution [1, 2]. Temperature is a key parameter to measure in a combustion process since it gives an indication of the overall combustion efficiency, heat release rate, chemical reaction rate and particle formation. Species concentration is then another key parameter. By providing experimental data to the numerical and kinetic models, a deeper understanding of how to increase the efficiency of the combustion process and lower the emission of pollutants can be obtained. With the gained knowledge, more efficient combustion reactors can be designed.

Optical techniques based on the nonlinear interaction between the laser radiation with the probed medium are known to provide sensitive measurements with high spatial resolution. This entails a momentary value of the studied parameter. Two of such techniques are degenerate four-wave mixing (DFWM) and laser-induced grating spectroscopy (LIGS), which are based on the four-wave mixing process and classified as laser-induced grating techniques. DFWM is a mature technique which has since the 1980s been employed in flames for species detection and concentration measurements [3, 4]. LIGS on the other hand, was in flame studies considered to be an interfering signal to the DFWM signal [5, 6] but has since the technical development showed to be a versatile technique used for measuring parameters such as temperature, speed of sound and thermal diffusion. On the contrary to many optical techniques, LIGS is better suited for high pressure environments, which was

[1] International Energy Agency, https://www.iea.org/data-and-statistics

demonstrated in [7]. The coherent nature of these techniques generates a signal beam which is laser-like and can therefore be guided away from the measurement object in order to supress the background light, from for example flames. The directivity of the generated signal beam facilitates the sensitive detection, since the whole signal can be guided to the detector. This feature makes the techniques especially useful for laser beams of non-visible wavelengths.

Combustion of the different fuels, both currently used and potential alternative fuels, lead to formation or release of important molecular species where some of them have strong absorption in the infrared spectral region but otherwise lack easily accessible transitions in the UV or visible region of the spectrum. Some of these molecules are small hydrocarbons like methane and ethylene, CO_2, water, hydrogen cyanide and ammonia, where the latter two are important precursors of the pollutant NO_x in biomass combustion.

Therefore, in order to be able to probe several of these molecules, the motivation of this work is to utilize the coherent nature of DFWM and LIGS and apply them in the infrared spectral region for concentration and temperature measurements in reactive flows, such as a flame. The work also included experimental improvement of the techniques in terms of sensitivity and applicability.

1.1 Outline of this thesis

This thesis is intended as an introduction to the subject and the laser-induced grating techniques used in Papers I-VI. Chapter 2 covers the basic principles of the two laser-induced grating techniques used in this work, namely laser-induced grating spectroscopy (LIGS) and degenerate four-wave mixing (DFWM). The experimental equipment used throughout the presented work is described in Chapter 3. Chapter 4 covers the temperature measurements performed both in heated gas flows and in flames using LIGS while Chapter 5 presents the concentration measurements performed using DFWM for detection of hydrogen cyanide and ammonia. Finally, conclusions and future perspectives of the techniques are discussed in Chapter 6.

2 Laser-induced grating techniques

2.1 Introduction to four-wave mixing

Four-wave mixing describes an optical process where three incident waves interact in a medium to generate a fourth wave [8, 9]. This interaction is achieved through an induced third-order polarization of the medium. The induced polarization, **P**, depends on the magnitude of the electric field, **E**, of the waves. For intense electric fields, the polarization can be expressed through a Taylor series expansion to include higher order nonlinear terms

$$\mathbf{P} = \chi^{(1)}\mathbf{E}_1 + \chi^{(2)}\mathbf{E}_1\mathbf{E}_2 + \chi^{(3)}\mathbf{E}_1\mathbf{E}_2\mathbf{E}_3 + \cdots \quad (2.1)$$

where $\chi^{(n)}$ is the nth-order susceptibility tensor. The four-wave mixing process can occur in a medium whose third-order susceptibility $\chi^{(3)}$ tensor is non-zero. The second-order susceptibility $\chi^{(2)}$ tensor also permits interaction of the electric fields but is zero in centrosymmetric medium, such as a gas.

The four-wave mixing techniques applied for gas spectroscopy requires sufficiently high electric field of the laser beams to generate the fourth field, being the signal beam. Moreover, the process is governed by the conservation of energy and momentum. Most four-wave mixing techniques fulfil this condition since there is no transfer of energy or momentum to the medium. Conservation of energy is achieved when the sum of the energies (and hence frequencies) of the interacting waves is zero, $\Delta\omega$=0, meaning that the frequency of the generated signal will be

$$\omega_4 = \omega_1 \pm \omega_2 \pm \omega_3 \quad (2.2)$$

Conservation of momentum, also referred to as phase-matching, is fulfilled when the wave vectors of the electric fields sum to zero, Δk=0, and the wave vector of the generated signal will be

$$\mathbf{k}_4 = \mathbf{k}_1 \pm \mathbf{k}_2 \pm \mathbf{k}_3 \quad (2.3)$$

The plus minus sign depends on the alignment geometry of the propagating wave vectors which fulfil the phase-matching condition. See section 2.1.1 for different alignment geometries.

Kiefer and Ewart [10] made an extensive review of the four-wave mixing techniques (often referred to as nonlinear techniques) used for combustion diagnostics. This

includes techniques such as Coherent Anti-Stokes Raman Spectroscopy (CARS), Polarisation Spectroscopy (PS), Degenerate Four-Wave Mixing (DFWM) and Laser-Induced Grating Spectroscopy (LIGS). The main advantage of these techniques is, due to their coherent nature where the signal is laser-like, the signal beam can be directed away from the measurement object and thus limit the background noise, from for example a flame, through spatial filtering. This enables sensitive detection with high spatial resolution, since the waves needs to be locally overlapped in order to achieve four-wave mixing. Their coherent nature facilitates the usage of laser beams with wavelengths outside the visible spectral range due to the beam directivity. In the following sections, the discussion is restricted to the main techniques of this thesis work, DFWM and LIGS. A more detailed discussion about these and other nonlinear techniques can be found in [10-12].

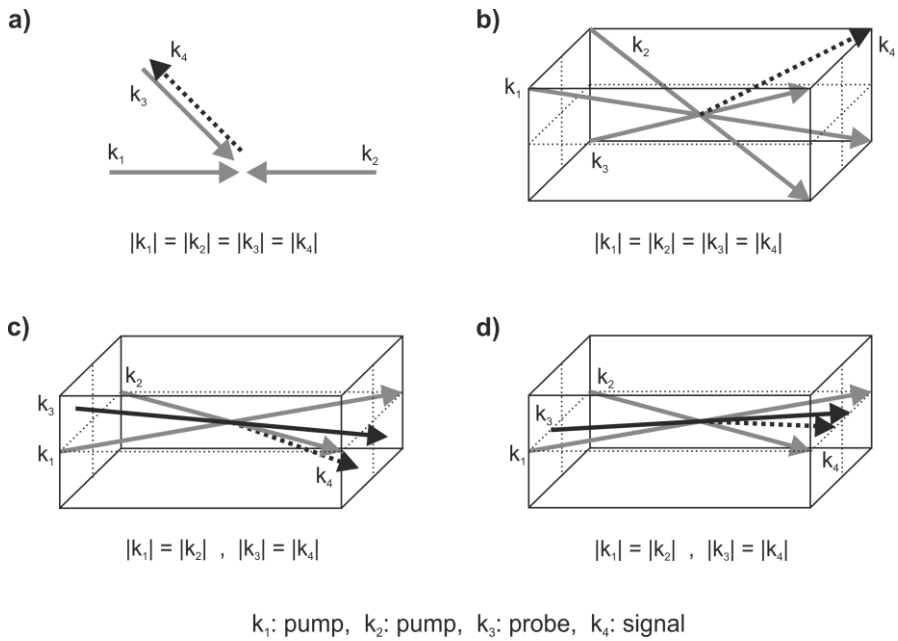

Figure 2.1. Alignment geometries for generating DFWM and LIGS signals together with the phase-matching condition that needs to be fulfilled. The laser beams noted here as k_1 and k_2 are pump beams, k_3 is probe beam and k_4 is the generated signal beam, which is represented as a black dashed arrow. An alignment approach for DFWM is presented in **a)** as phase conjugate geometry and **b)** as forward phase-matching in folded BOXCARS configuration. Forward phase-matching alignment geometries for LIGS are presented in **c)** as folded BOXCARS and **d)** as planar BOXCARS.

2.1.1 Alignment geometry

Figure 2.1 shows different alignment geometries in order to generate DFWM and LIGS signals, along with the phase-matching condition which needs to be fulfilled.

The alignment geometries associated with DFWM are illustrated in a) and b), where a) shows the phase conjugate geometry, also referred as backward pump geometry, where two of the laser beams which are acting as pump beams are counter-propagating. The three-dimensional alignment geometry for DFWM is shown in b) as the forward phase-matching in the folded BOXCARS configuration. The forward phase-matching geometries for LIGS are presented in c) as folded BOXCARS and d) as planar BOXCARS configuration, where in the latter all laser beams are aligned in the same horizontal plane. The geometries illustrated in b)-d) were used throughout the experimental work presented in this thesis.

2.2 Degenerate four-wave mixing (DFWM)

Degenerate four-wave mixing is a special case of four-wave mixing where the three input laser beams and the generated signal beam have the same (degenerate) frequency. It was first described by Abrams and Lind [13, 14] and followed by several theoretical and experimental investigations concerning the effects of saturation [15-18], polarization [18] and spectral broadening [19-21].

As a diagnostic technique it has shown to be a powerful absorption technique for detection of minor species. The first implementation of DFWM for combustion diagnostics was performed in laminar flames to detect sodium atoms [3] and the hydroxyl radical (OH) [4] using the phase conjugate geometry. The forward phase-matching geometry provides relatively higher DFWM signals [22] and was first demonstrated in flames by detecting OH [23].Two-dimensional OH measurements have been performed [24, 25] and DFWM has also been applied for temperature measurements [26-28]. Sun *et al.* presented an approach for thermometry in flames where the ratio between two group of temperature sensitive water lines are utilized [29].

Mid-infrared DFWM has in previous work been used to detect CO_2 [30], HF [31], CH_3Cl [32], HCl [33, 34], small hydrocarbons like CH_4 [30, 35, 36], C_2H_2 [30, 34-37], C_2H_6 [36], CH_3OH [32], and nitrogen containing species NO_2 [33] and N_2O [30]. The list of the latter molecular species has been expanded to include HCN [38] and NH_3 [39] through this thesis work, as summarized in Papers V and VI. In the following sections, the principles of DFWM is briefly covered together with an applied simulation model of the DFWM

2.2.1 Principles of DFWM

The process of the generation of a DFWM signal can be represented with a grating picture [10]. Two of the laser beams, acting as pump beams, are crossed with the

crossing angle θ between the beams to form an interference pattern. Since the laser wavelength is resonant with the absorbing species, it leads to a spatial periodic variation in the excited state population of the probed molecular species, known as a population grating. The spacing between the grating planes, Λ, is given by

$$\Lambda = \frac{\lambda_{pump}}{2\sin(\theta/2)} \tag{2.4}$$

where λ_{pump} is the laser wavelength. A third beam, acting as probe beam, is scattered off of the grating to form a signal beam. For optimal scattering, the third beam is aligned to intersect the grating at the Bragg angle, θ_B,

$$\sin(\theta_B) = \frac{\lambda_{probe}}{2\Lambda} \tag{2.5}$$

In DFWM the probe wavelength, λ_{probe}, is the same as the pump wavelength, which means that the Bragg angle is half the crossing angle.

Abrams and Lind presented in 1978 the analytical expression for DFWM [13, 14] and it is the commonly used model for DFWM. It assumes phase conjugate geometry, a stationary two-level absorber, an optical thin medium and monochromatic laser beams where all have the same polarization and the probe beam has non-saturating intensity. Based on these assumptions, the analytical expression for the DFWM signal intensity is as follows [12]

$$I_{DFWM} = \frac{\alpha_0^2 L^2}{1+\delta^2} \cdot \frac{4\left(I_{pump}/I_{sat}\right)^2}{\left(1+4I_{pump}/I_{sat}\right)^3} I_{probe} \tag{2.6}$$

where L is the interaction length, I_{pump} is the intensity of the pump laser beam, I_{probe} is the intensity of the probe laser beam, I_{sat} is the saturation intensity. The line centre absorption coefficient $\alpha_0$and the normalized detuning δ are expressed below together with I_{sat}.

$$I_{sat} = \frac{\hbar^2 c \epsilon_0}{2\tau_1 \tau_2 \mu^2}(1+\delta^2) \tag{2.7}$$

$$\delta = (\omega - \omega_0)\tau_2 \tag{2.8}$$

$$\alpha_0 = \frac{\mu^2 \Delta N_0 k \tau_2}{2\epsilon_0 \hbar} \tag{2.9}$$

Here, ϵ_0 is the vacuum permittivity, τ_1 and τ_2 are the population and coherence dephasing relaxation times, respectively, μ is the transition dipole moment, c is the speed of light, k is the magnitude of the wave vector, ω_0 is the line center frequency, ΔN_0 is the difference in population between the upper and lower energy levels in the absence of an applied field.

The signal intensity of Eq. 2.6 depends on the degree of saturation of the pump beams, which in turn is a function of the detuning, dipole moment and relaxation times. The absorption coefficient depends on the dipole moment, coherence relaxation time and the number density. Assuming that the laser intensity for the pump and probe is the same (I), and inserting Eqs. 2.7-2.9 into Eq. 2.6, the DFWM signal intensity [12] can be expressed as for unsaturating laser intensity I,

$$I_{DFWM} \propto \mu^8 N^2 L^2 \tau_1^2 \tau_2^4 \cdot \frac{1}{(1+\delta^2)^3} \cdot I^3, \;\; I \ll I_{sat} \tag{2.10}$$

and for saturating laser intensities

$$I_{DFWM} \propto \mu^2 N^2 L^2 \frac{\tau_2}{\tau_1}, \;\; I \geq I_{sat} \tag{2.11}$$

where N is the total number density in the gas. As noted from Eq. 2.7, the saturation intensity depends on the detuning from the line center, which implies that the degree of saturation varies across the absorption line. The line integrated DFWM signal is of interest in many diagnostic applications, where the signal is expressed as [12]

$$I_{DFWM,int} \propto \mu^8 N^2 L^2 \tau_1^2 \tau_2^3 I^3, \;\; I \ll I_{sat}^0 \tag{2.12}$$

$$I_{DFWM,int} \propto \mu^3 N^2 L^2 \sqrt{\frac{\tau_2}{\tau_1}} I^{1/2}, \;\; I \geq I_{sat}^0 \tag{2.13}$$

Here, I_{sat}^0 is the saturation intensity at line center. For unsaturating laser beams, the signal intensity is proportional to the cube of the laser intensity. For both cases, the signal is proportional to the square of the total number density of the probed species. As it can be seen in the expressions above for saturating and unsaturating DFWM signal intensities, the Abrams and Lind model predicts the signal dependence on the transition dipole moment (μ) to be different depending on the degree of saturation. This has been experimentally investigated for the NO DFWM signal in flames [40].

For concentration measurements, it is preferable to use saturating laser intensities, since the saturated DFWM signal is less dependent on relaxation times, collisional quenching and fluctuations in laser intensity [16, 41]. However, the Abrams and Lind model does not consider both saturating probe and pump beams. Therefore, a model is needed which is valid for more general cases. A numerical solution has been proposed [15] which is based on calculations of the time-dependent density-matrix, but is time consuming. A general analytical expression of the DFWM signal has been proposed by Bratfalean et al. [17], where it has been shown to work for simulations of saturating DFWM signals of closely spaced lines [42].

2.2.2 Simulation of the DFWM spectrum

The simulation of the DFWM spectrum is based on a simplified empirical relation retrieved from the theoretical analysis in [13, 14, 40]

$$I_{DFWM} \propto \sigma(\nu)^2 N^2 \tag{2.14}$$

where σ(ν) is the absorption cross section for the wavenumber *ν*, and *N* is the number density of the gas. This assumes the relation $\sigma^2 \propto \mu^4$, which is a good assumption for pump laser intensities above the saturation level [40]. It assumes that the relaxation times and collisional effects are the same for all lines within the simulated spectral range and that the fluctuation in the laser pulse energy is negligible. This relation is primarily used for spectral line identification and not for quantitative measurements. Taking into account the absorption cross section for every transition, the relation for the simulated DFWM signal becomes

$$I_{DFWM} \propto \left(\sum_i S_i g(\nu) \right)^2 N^2 \tag{2.15}$$

where S_i is the line strength and $g(\nu)$ is the line shape. The line strength is throughout this work retrieved from the HITRAN or HITEMP databases [43, 44]. As an example, Figure 2.2 shows the mid-infrared DFWM spectrum of 0.99 % ammonia in N_2 recorded at room temperature. A simulation of the NH_3 mid-IR DFWM spectrum based on Eq. 2.15 is included for qualitative comparison. The intensity of the simulation has been adjusted to match the measured spectrum. Overall, there is a good agreement between the spectra except between 4400-4450 cm^{-1} where there are some lines missing in the simulation due to incomplete data in the HITRAN database.

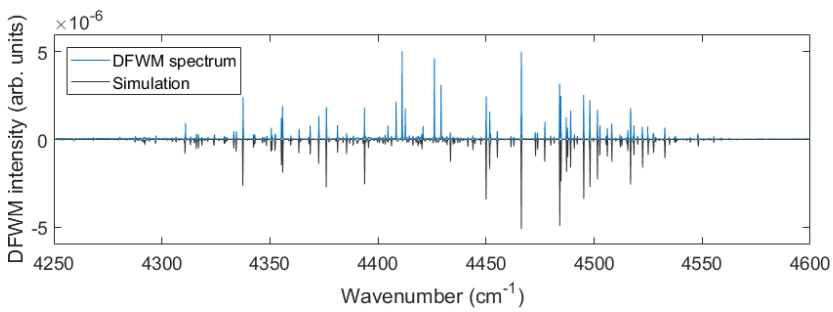

Figure 2.2. Mid-IR DFWM spectrum of ammonia recorded in a gas flow mixture containing 0.99 % ammonia diluted in N_2 at 296 K. Simulation of the mid-IR DFWM spectrum of ammonia is included for comparison.

2.2.3 Concentration measurements using DFWM

In order to perform quantitative concentration measurements with DFWM, the temperature and concentration dependence of the DFWM signal needs to be known. For the work presented in section 5.2 and Paper V, the following model is proposed for the concentration (c) dependence of the signal, which varies with temperature (T)

$$I_{DFWM}(T,c) = as(T)c^2 + b \tag{2.16}$$

where a is an experimental constant which takes into account any variables that depend on the particular experimental setup. This includes such as the efficiency of the detector, crossing overlap of the DFWM alignment and material constants as reflectivity and transmission of the used optics. The offset b represents the mean value of the background noise from scattered light. The scaling factor $s(T)$ is the expansion of the simplified empirical relation in Eq. 2.14, which describes the DFWM signal as the convolution between the spectrum obtained from Eq. 2.14 and the line shape of the pump laser

$$I_{DFWM} \propto s(T) = \int_{\nu_l}^{\nu_u} \left(\sigma(T,\nu)N(T)\right)^2 L(\nu,\nu_0)d\nu \tag{2.17}$$

Here, L is an estimate of the laser line shape centered at ν_0 and the upper and lower bound of the integral, ν_u and ν_l chosen to be wide enough to cover the probed absorption line used for concentration measurements. The integral needs to be evaluate as a function of temperature since the line shape of the absorption line changes with temperature, thus resulting in a change of the overlap with the laser line.

2.3 Laser-induced grating spectroscopy (LIGS)

Laser-induced grating spectroscopy is a four-wave mixing technique based on having two incident laser beams with the same frequency (which acts as pump beams), while the third incident laser beam has a different frequency. The generated LIGS signal beam has the same frequency as the third beam. The technique is closely related to DFWM, but instead of a population grating, the dynamics of a grating formed by collisional relaxation of excited molecular species leading to local heating (*thermalization*) or by compression of the molecules by the high electric field of the pump laser beams (*electrostriction*) is studied. These underlying concepts for LIGS are discussed in section 2.3.1.

LIGS is a versatile laser diagnostics technique mainly used for measuring temperature [45-49] but also speed of sound [49-51], thermal diffusivity [52], flow

velocity [53-55] and pressure [56-58]. LIGS has also been applied for local concentration measurements [59, 60] and molecular relaxation processes [61-65]. Two-dimensional measurement using electrostrictive LIGS has been demonstrated by Hemmerling and Stampanoni-Panariello [66]. The latest development of LIGS concerns the use of high repetition rate lasers as pump laser beams [67, 68] and performing multi-point measurement by extending LIGS from a point to a one dimensional (1-D) line [69].

Our research group focuses on the development and application of mainly mid-IR LITGS [70] where fundamental ro-vibrational transitions of combustion-related molecular species can be probed. The work covered in Papers I-III expands the contributions of mid-IR LITGS [71, 72]. Furthermore, we expanded the work to include infrared O_2 LIGS as summarized in Paper IV.

2.3.1 Principles of LIGS

A brief overview of the principles of laser-induced grating spectroscopy is covered here and for a more mathematical treatment the reader is advised to visit for example [10, 49, 73-76].

As for DFWM, two high power laser beams of same frequency are aligned to cross at an angle θ. The interference between these two beams defines the probe volume and it creates a sinusoidal spatial variation in intensity. These fringes of high and low intensity form parallel planes which constitutes a grating with spacing Λ as defined in Eq. 2.1. The grating spacing is determined by the pump laser wavelength, λ_{pump}, and crossing angle θ. In order to create a laser-induced *thermal* grating (LITG), the wavelength of the pump laser beams is chosen to be resonant with an absorption transition of the target molecular species present in the probe volume. Excitation of the target molecules to higher energy levels occur along the high intensity fringes. Subsequent de-excitation mainly through collisions with surrounding molecules in the probe volume result in local heating of the bulk gas. This process is also known as thermalization and leads to formation of two density perturbations. The localized heating results in a small temperature rise which reduces the gas density in the high intensity fringes. This generates a thermal grating which decays exponentially due to thermal diffusion. The second density perturbations arise from the pressure changes due to the spatial density modulation caused by rapid heating. This results in formation of two counter-propagating acoustic waves, which propagate orthogonal to the thermal grating planes and decay exponentially due to viscous damping. The sum of the acoustic waves is a standing acoustic wave. As a result, the total density perturbation is a sum of these two contributions, where the strength of the thermal grating is modulated in time by the oscillations from the acoustic waves. The acoustic waves cause a time-evolving

oscillation of the refractive index, which oscillates at the frequency f_{osc} accordingly [49],

$$f_{osc} = \frac{v_s}{\Lambda} \tag{2.18}$$

where v_s is the speed of sound of the gas in the probe volume. The dynamics of the laser-induced grating can be detected by a third laser beam, acting as probe beam, to follow the time evolution of the grating formation. The probe beam of wavelength λ_{probe}, is aligned at the first Bragg angle, θ_B, in order to satisfy the Bragg diffraction condition according to Eq. 2.2. Figure 2.3 shows the principle of generation of a laser-induced thermal grating (LITG) and detection of it as described above.

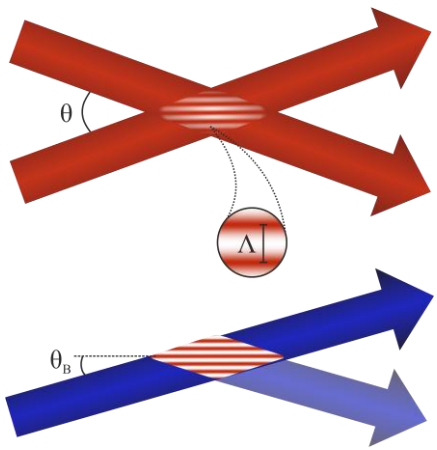

Figure 2.3. Schematic principle of formation of the thermal laser-induced grating (LITG). After the formation of a light interference pattern by the pump beams (red) and target species absorption, the susequenct thermalization results in thermal and acoustic gratings with grating spacing Λ. The dynamics of the gratings is probed using a probe beam (blue) which is aligned to intersect the gratings at the first Bragg angle. This results in Bragg diffraction of the probe beam, which is the signal beam.

Laser-induced *electrostrictive* gratings (LIEG) are on the other hand formed through electrostriction by non-resonant pump beams with high pulse energies [74, 77, 78]. The high electric field of the pump laser beams causes a compression of the gas towards the high intensity fringes in the interference pattern. This results in a density modulation and hence a generation of acoustic waves. Since the stationary thermal grating is negligible or not present, a pure LIEGS signal consists only of the acoustic waves travelling out of the probe volume. This means that these signals oscillate at twice the frequency compared to the signals from a thermal grating. However, the signal intensity is common to be lower for a LIEGS signal compared to a resonant LITGS signal.

2.3.2 Temperature measurements using LIGS

The oscillation frequency in the LIGS signals can be used to determine the speed of sound, v_s, of the probed medium [50, 79, 80], since it depends on the speed of sound and the grating spacing as expressed in Eq. 2.18. Gas has been the probed medium throughout this work, and thus it is the focus of the discussion henceforward. The speed of sound for a gas depends on the composition and the temperature according to the following relation

$$v_s = \sqrt{\frac{TR\gamma}{M_{gas}}} \tag{2.19}$$

where M_{gas} is the mean molar mass of the gas, γ is the specific heat ratio of the gas, R is the universal gas constant and T is temperature. By combining Eqs. 2.18 and 2.19, the gas temperature of the probe volume can be calculated as

$$T = \frac{f_{osc}^2 \Lambda^2 M_{gas}}{R\gamma} \tag{2.20}$$

This implies that the temperature can be determined from the oscillation frequency in the LIGS signals, based on that the gas composition is known. The requirement on knowing the gas composition is a challenge in applications where the composition consists of a vast molecular species, such as in flames. However, in many cases it is sufficient to have an estimate of the major molecular species constituting the bulk gas, especially if the molecules have similar thermophysical properties, such as thermal diffusivity. The estimation of the gas composition in flames can be based on existing literature or models of the chemical kinetics and information about the specific heat ratio can be obtained from [81]. Moreover, the temperature calculation also depends on the accurate determination of the grating spacing. This can be achieved by recording the LIGS signal in a calibration gas under known conditions to obtain the oscillation frequency and calculate the grating spacing.

An example of LITGS signals at different temperatures are shown in Figure 2.4. These are LITGS signals from water molecules recorded at 3284 cm^{-1} in a heated gas flow mixture of water and nitrogen. The inset shows the power spectrum of the signals obtained through fast Fourier transform (FFT), which reveals the oscillation frequency. With increasing gas temperature, the speed of sound, and hence the oscillation frequency, increases. This can also be deduced from the equations above.

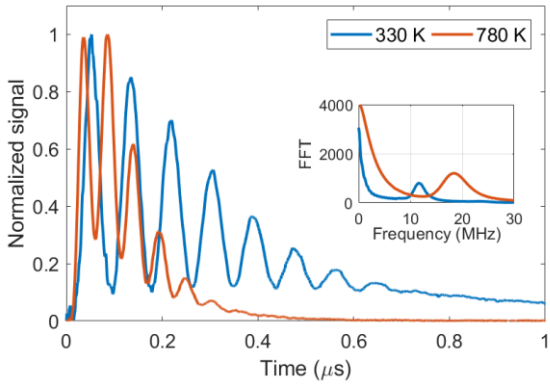

Figure 2.4. Normalized LITGS signals of water recorded at 3284 cm^{-1} in a heated gas flow containing water and nitrogen. Signals recorded at two different temperatures are shown. The inset displays the Fourier transform of the two signals, which indicates their oscillation frequency.

2.3.3 Acoustic damping and thermal diffusivity

The oscillatory part of the signal is attributed to the standing acoustic waves propagating out of the probe volume, and the decay of the oscillations is characterized by the time constants of acoustic damping time and acoustic transit time. The acoustic waves decay exponentially due to viscous damping and the time of decay is given by the acoustic damping time, τ_a, [82-84] which can be calculated as

$$\tau_a = 2\left(\frac{\Lambda}{2\pi}\right)^2 \left\{\frac{1}{\rho}\left[\frac{4}{3}\mu + (\gamma - 1)\cdot\frac{\kappa}{c_p}\right]\right\}^{-1} \tag{2.21}$$

where, μ is the dynamic viscosity, ρ is the density, κ is the thermal conductivity, c_p is the specific heat at constant pressure, and $\gamma = c_p/c_v$ is the ratio of specific heats at constant pressure and volume.

As the probe volume is not infinite in size, the acoustic waves will travel out of the volume during the lifetime of the LIG. The oscillations will then also decay exponentially due to the acoustic transit time τ_{tr} [74] which depends on the beam radius w at the probe volume and the speed of sound as

$$\tau_{tr} = \frac{w}{\sqrt{2}v_s \cos(\theta/2)} \approx \frac{w}{\sqrt{2}v_s} \tag{2.22}$$

In practical LIGS experiments where focused pump laser beams are used, the probe volume is small enough that the acoustic transit time can be smaller than the acoustic damping. In that case, the viscous damping can be neglected since its contribution to the exponential decay of the acoustic waves is slower.

The stationary thermal part of the laser-induced grating (LIG) decays exponentially according to thermal diffusion of the gas. The time constant for this decay, τ_{th}, is given by

$$\tau_{th} = \left(\frac{\Lambda}{2\pi}\right)^2 \chi^{-1} \tag{2.23}$$

where $\chi=\kappa/\rho c_p$ is the thermal diffusivity. This means that small grating spacings result in short thermal diffusion time constants, which lead to fast exponential decays of the thermal LIG and hence, shorter signals.

2.3.4 Simulation of the LIGS signal

The empirical simulation model for the LIGS signals adopted in this work is based on the approach from Kozlov *et al.* [61, 84]. It has been mostly adopted for LITGS of the O_2 $\left(b^1\Sigma_g^+\right)$ excited state in order to associate the origin of the different molecular energy transfer contributions (electronic, rotational, vibrational) to the signal [61, 62, 64]. The model is derived by solving the linearized hydrodynamic equations which describes the change in gas density and temperature due to heating, under the assumption of weak damping of the acoustic waves [61, 64, 84, 85].

The model for excited O_2 molecules assumes a three-stage energy transfer with the medium; rotational, electronic and vibrational. The rotational relaxation was assumed to be instantaneous, meaning that it occurred on a time scale shorter than the duration of the pump laser pulse. The electronic and vibrational relaxations were attributed to occur during a finite time scale, τ_f, which is longer than the pump laser pulse duration, contributing to a fast and slow energy relaxation, respectively.

Within the scope of this thesis work, the applied general model considers an instantaneous ($I_i(t)$) and finite time ($I_f(t)$) energy transfer. In the presence of strong electric fields of the pumps laser beams, the contribution from electrostriction needs to be considered ($I_e(t)$). This leads to the following model

$$I(t) \cong \left(I_i(t) + I_f(t) + I_e(t)\right)^2 \tag{2.24}$$

where the contribution from the instantaneous energy redistribution is

$$I_i(t) = M_i\left(cos(2\pi f_{osc}t) \cdot e^{(-(t/t_{tr})^2-(t/\tau_a))} - e^{(-t/\tau_{th})}\right) \tag{2.25}$$

The finite time energy redistribution is

$$I_f(t) = M_f \left(\left(\frac{k_f}{1+k_f^2} sin(2\pi f_{osc} t) + \frac{1}{1+k_f^2} cos(2\pi f_{osc} t) \right) \times \right.$$
$$\left. e^{(-(t/t_{tr})^2 - (t/\tau_a))} - \frac{e^{(-t/\tau_{th})} - e^{(-t/\tau_f)}}{\tau_f(1/\tau_f - 1/\tau_{th})} - \frac{1}{1+k_f^2} e^{(-t/\tau_f)} \right) \quad (2.26)$$

and the electrostrictive contribution is

$$I_e(t) = M_e sin(2\pi f_{osc} t) \cdot e^{(-(t/t_{tr})^2 - (t/\tau_a))} \quad (2.27)$$

Here, M_i, M_f and M_e are dimensionless coefficients which scales the different contributions to the laser-induced grating, f_{osc} is the oscillation frequency and the constant k_f is defined as $k_f = 2\pi f_{osc}\tau_f$, where τ_f is the characteristic finite energy transfer time. The decay of the oscillations in the LIGS signal are described by the acoustic transit time (τ_{tr}) and the acoustic damping time (τ_a). However, the acoustic transit time is considered to the dominant factor in the exponential decay of the oscillations, thus the acoustic damping time is not considered in the simulations. The dissipation of the thermal grating is governed by thermal diffusion (τ_{th}).

In this work, the fitting of the simulation model to the experimental LIGS signals has been mainly applied to extract the precise oscillation frequency in order to retrieve the gas temperature for thermometry applications, as described in section 2.3.2. No attempt has been made to fully understand the relaxation process of the different probed molecules.

2.3.5 Experimental considerations

Selection of laser wavelength for pump and probe beams

In general, the wavelength of the probe and pump laser beams can be arbitrary. However, a pulsed laser should be chosen as the pump laser beams in order to create a dynamic grating which resolves after each laser pulse. Moreover, a continuous-wave (CW) laser is beneficial to be used as the probe laser beam to capture the whole time evolution of the LIGS signal. A long-pulsed laser can also be used as the probe beam, where it scans across the LIGs in time to obtain different segments which are patched together. For a laser-induced grating based on electrostriction, it requires a pump laser with high pulse energy but the pump laser wavelength can be arbitrarily chosen, which enables the use of lasers with fixed wavelengths. A laser-induced thermal grating requires a pump laser with tuneable wavelength which can be tuned to a resonant transition of the target molecular species. It is beneficial if the probe laser wavelength is different from the pump laser wavelength, and also any other laser wavelengths used to pump the main laser system which provide the

pump laser beams in a LIGS experiment, in order to avoid any possible background scattering or overlap with the signal beam.

Most efficient scattering is achieved for low ratio values between the probe and pump wavelengths [82],

$$\frac{\lambda_{probe}}{\lambda_{pump}} = \frac{\sin(\theta_B)}{\sin(\theta/2)} \tag{2.28}$$

where $\theta_B < \theta$. This means that the laser wavelengths have a large spectral separation and the Bragg angle is small, leading to a long interaction path between the LIG and the probe beam which result in efficient scattering and hence strong signals. However, for pump laser beams with wavelengths in the UV spectral region, it becomes impossible to align a probe beam to satisfy $\theta_B < \theta$. Instead, the probe laser wavelength is chosen to be longer than the pump laser wavelength, thus resulting in a Bragg angle of the probe laser beam larger than the crossing angle.

Resolved oscillation peaks

The uncertainty in determining the oscillation frequency depends on the number of resolved oscillation peaks in the LIGS signal. More resolved peaks lower the uncertainty in the frequency determination and it can be achieved by increasing the width of the probe volume, which increases the acoustic transit time of the propagating acoustic waves across the probe volume.

For practical LIGS experiments using focused beams, the width of the probe volume is determined by the diameter of the focus of a Gaussian beam ($2w$) which depends on the pump wavelength λ_{pump}, the focal length of the lens f, and the beam diameter before the focusing lens $2w_0$ as

$$2w = 4\frac{\lambda_{pump}}{\pi} \cdot \frac{f}{2w_0} \tag{2.29}$$

where w is the radius of the Gaussian laser beam. However, a wider probe volume leads to a decrease in spatial resolution, thus resulting in a trade-off between spatial resolution and acoustic transit time, and therefore number of resolved oscillations in the signal. Furthermore, for efficient diffraction of the probe beam, Hemmerling *et al.* [86] expressed that the following Bragg diffraction requirement which needs to be satisfied

$$\frac{w}{\Lambda} > \frac{1}{2\sqrt{2}\left(\lambda_{probe}/\lambda_{pump}\right)} \tag{2.30}$$

where w is the pump beam radius at focus and Λ is the grating spacing. This indicates how many grating planes are needed in order to have efficient Bragg diffraction of the probe beam.

3 Experimental equipment

3.1 Lasers

The work presented in this thesis used a narrowband laser system consisting of an injection-seeded Nd:YAG laser, a dye laser and a frequency conversion unit in order to generate infrared laser radiation. Figure 3.1 shows a schematic overview of the laser system. The second harmonic of the Nd:YAG laser output (532 nm) is used to pump a dye laser which generates a laser beam with tuneable wavelength. The dye laser beam can itself be used for near-infrared experiments. However, it can also be difference-frequency mixed in the frequency conversion unit with the fundamental Nd:YAG laser output (1064 nm) left from the second harmonic generation in order to generate a mid-infrared laser beam. The laser system is used for scanning or on-line measurements by tuning the dye laser wavelength and operates at 10 Hz. The different components of this laser system are described in more detail in sections 3.1.1-3.1.3.

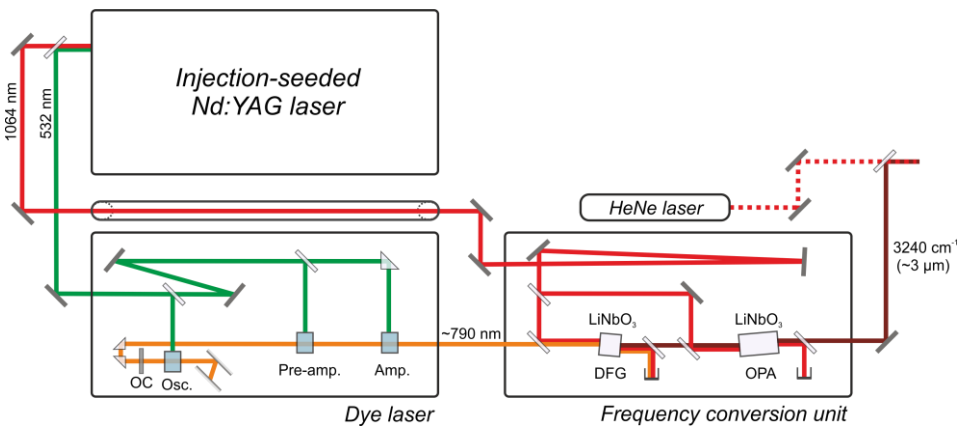

Figure 3.1. Schematic overview of the infrared laser system, which consists of an injection-seeded Nd:YAG laser, a dye laser and a frequency conversion unit. The frequency-doubled output from the Nd:YAG laser (532 nm) is used to pump the dye laser, which produces a dye laser beam of tuneable wavelength. In the frequency conversion unit the dye laser is difference-frequency mixed with the fundamental Nd:YAG laser output (1064 nm) in order to generate mid-infrared laser radiation.

3.1.1 Nd:YAG laser

The Nd:YAG laser is the most commonly used high-power pulsed laser system. It is a solid-state laser where the gain medium is a neodymium-doped yttrium aluminium garnet crystal, Nd:$Y_3Al_5O_{12}$. Its fundamental wavelength is 1064 nm and through frequency conversion the 2nd, 3rd and 4th harmonic can be reached, which corresponds to 532 nm, 355 nm and 266 nm, respectively.

A single-longitudinal-mode Nd:YAG laser (Spectra-Physics, Quanta-Ray PRO 290-10) is used in the infrared laser system. Its single-longitudinal mode operation is achieved through injection seeding by a narrowband CW seed laser of model 6350, which results in a narrow linewidth of <0.003 cm^{-1}. It runs at a repetition rate of 10 Hz and has a pulse duration of 8-10 ns. The pulse energy of the fundamental output is around 1.5 J and its current configuration is to undergo frequency conversion in order to produce the 2nd harmonic. The residual 1064 nm beam from the second harmonic generation is used in the difference-frequency mixing process in the frequency conversion unit, while the 532-nm beam is used to pump the dye laser. The pulse energy of the 532-nm beam is around 750 mJ.

The good beam profile of the 1064 nm beam is preserved for mixing in the frequency conversion unit by imaging the beam at laser output by two plano-convex lenses with a focal length of 750 mm. The 1064 nm beam needs then to pass through a relay vacuum tube with Brewster windows in order to avoid breakdown in air.

3.1.2 Dye laser

Dye lasers are commonly used as tuneable laser sources, where the active medium is a dye solution that provides a continuous tuneable wavelength range. The dye solution consists of an organic dye in a liquid solvent and depending on the type of organic dye, different wavelength regions can be accessed. The dyes LDS 722 (Pyridine 2), LDS 765 and LDS 798 (Styryl 11) have been used and the solvent throughout all experiments was ethanol.

The Sirah dye laser (PrecisionScan PRSC-D-18) used in this work is pumped with the above-mentioned Nd:YAG laser at 532 nm. The oscillator cavity consists of two gratings with 1800 lines/mm, which allows to achieve a linewidth narrower than 0.04 cm^{-1} at 625 nm, and a tuning range of 410-900 nm. The whole tuning range is accessed by changing the dye solution. Although it has a narrow linewidth, the dye laser output consists of 2-3 longitudinal modes which can affect the reproducibility of the measurements, especially when it jumps between the number of modes. Therefore, the dye laser has recently been equipped with a dynamic operational mode (DMO) of the out coupling (OC) mirror, which vibrates the dye laser cavity in order to increase the randomness of the longitudinal mode structure. This solution

provides more reproducible excitation scans. Finally, the dye laser consists of two amplification stages and delivers a pulse energy of 60 mJ at 800 nm.

3.1.3 Frequency conversion unit

The Sirah dye laser system described above is equipped with a frequency conversion unit (OPANIR) which can either be used for frequency doubling or difference-frequency generation (DFG). Mid-IR laser radiation is achieved by difference-frequency mixing of visible/near-infrared light with the 1064 nm laser radiation accordingly

$$\lambda_{IR} = \frac{1}{\left|\frac{1}{\lambda_{1064}} - \frac{1}{\lambda_{Dye}}\right|} \tag{3.1}$$

The dye laser output and a part of the remaining fundamental output from the Nd:YAG laser is mixed in a temperature regulated lithium niobate ($LiNbO_3$) crystal, working on the principle of DFG. The resulting mid-IR laser radiation has a wavelength between 1.4 µm and 5.2 µm, depending on the dye laser wavelength. The whole mid-IR wavelength range is covered by three different crystals since the coverage depends on the cut angle of the crystals. Throughout all the experiments presented in this thesis, a $LiNbO_3$ crystal with the wavelength range of 1.8-4.2 µm was used. The generated mid-IR laser beam is mixed with another part of the 1064 nm laser beam in a second temperature regulated $LiNbO_3$ crystal, functioning as an optical parametric amplifier (OPA), in order to increase the pulse energy of the mid-IR beam. Typical pulse energy at 3 µm is 7 mJ and the pulse duration of around 4 ns results in a long coherence length which enables simple and straightforward alignment of the laser-induced grating techniques based on splitting of the initial mid-IR laser beam. During excitation scans, the angle of the $LiNbO_3$ crystals is automatically adjusted while scanning the dye laser wavelength in order to preserve the phase-matching condition between the mixing laser beams.

The resulting linewidth of the mid-IR laser pulses are governed by the dye laser linewidth since it is broader than the Nd:YAG laser linewidth. The full width at half maximum (FWHM) linewidth of the mid-IR laser pulses has been measured to be 0.025 cm^{-1} at 2.7 µm when investigating the laser-induced fluorescence excitation scan of CO_2 in a gas cell at 10 mbar [87].Since the mid-IR laser beam is invisible for the human eye, a HeNe laser beam (632 nm) is spatially overlapped with the mid-IR laser beam in order to ease the alignment of the mid-IR laser beam during experiments. In addition to this, temperature-sensitive thermochromic liquid crystal papers were used to trace the mid-IR laser beam. The diameter of the mid-IR beam is around 3 mm.

3.1.4 DPSS laser

In all LIGS experiments a continuous-wave (CW) diode-pumped solid state (DPSS) laser (Laserglow Tech., LRS-0457) was used as probe laser. Its operational wavelength of 457 nm is obtained by the second harmonic of the diode-pumped Nd:YVO_4 crystal and has an output power of 200 mW. The beam diameter is 3 mm with a near TEM_{00} mode and it has a spectral linewidth of <0.2 nm. This small and compact laser was oriented to have orthogonal polarization to the LIGS pump laser beams in order to obtain strongest possible diffracted signal.

3.2 Optical components

3.2.1 Optical material

When selecting optics made of a certain optical material there are a few factors that needs to be taken into consideration, such as high transmission or reflectance for the applied wavelength, damage threshold and material cost.

Lenses and beamsplitters made of UV-grade fused silica (FS) were used during experiments that involved laser radiation with wavelengths in the visible/near-IR spectral regions. Silver mirrors were extensively used due to their high reflectivity in these wavelength regions. However, these optical materials have poor performance in the mid-IR spectral region. Therefore, most mid-infrared optics used in the experiments as lenses, beamsplitters or dichroic mirrors are made of CaF_2 or MgF_2. Few optical components are made of IR-grade FS, which transmits well up to 2.7 μm and windows made of sapphire were used due to its good mechanical properties. Gold mirrors were preferred due to its slightly higher reflectivity in mid-IR. The transmission curves of the used optical materials are shown in Figure 3.2.

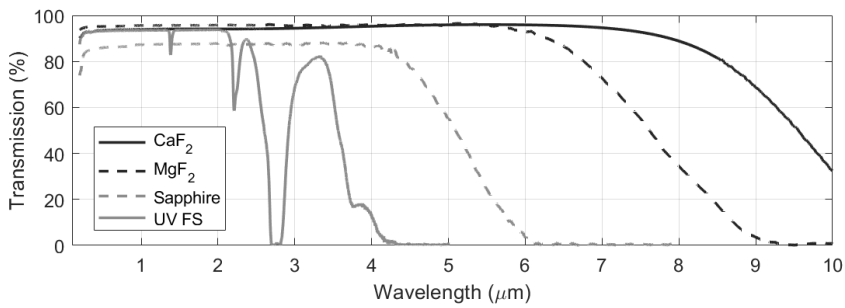

Figure 3.2. Transmission curves for the commonly used optical materials retrieved from Thorlabs [88]. All transmission curves are made for 5 mm thick windows except for UV-grade fused silica (FS) which is obtained for a window thickness of 10 mm.

3.2.2 BOXCARS plates

In order to setup a DFWM experiment, three laser beams of equal intensities are needed. For this purpose, a set of sophisticated beamsplitters (called BOXCARS plates) were used to split a single beam into four parallel beams. Three of these beams were used during the mid-IR DFWM measurements to achieve the forward phase-matching condition in the folded BOXCARS configuration.

The set consists of two identical, specially coated plates with the dimension 50×50×15 mm^3. The coating consists of a combination of anti-reflection, 50 % reflectance and high reflectance (> 99 %) layers. Figure 3.3 shows a schematic drawing of the BOXCARS plates where the different coating areas are indicated. The first plate is titled at an angle of 45° with respect of the beam propagation axis. The beam propagates through the anti-reflection coated input surface and undergoes the first internal reflection by the 50 % reflecting output surface, which serves as a 50/50 beamsplitter. Part of the beam pass through the surface whilst the other part is reflected towards the high reflection surface, where it undergoes the second internal reflection followed by transmission through the anti-reflection coated output surface. This results into two parallel beams with nearly equal intensity. Each beam is then split into two beams using the second plate, which is tilted at an angle of 45° around the axis perpendicular to the beam propagation. In this way, the BOXCARS plates split one laser beam into four laser beams symmetrically placed as the corners of a square with the distance of 12 mm.

Two different sets of BOXCARS plates were used for the mid-IR DFWM measurements. During the detection of ammonia at 2.3 µm, the BOXCARS plates made of IR-grade fused silica with coatings designed for operation in the wavelength range 1.9-2.5 µm were utilized. For the hydrogen cyanide measurements, the BOXCARS plates made of CaF_2 with coatings covering 2.7-3.3 µm were used instead.

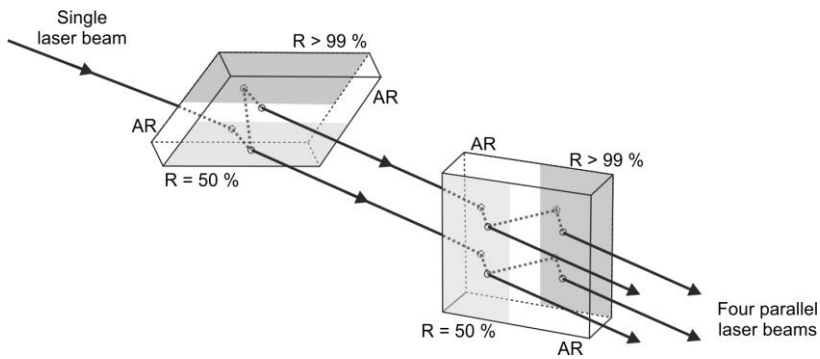

Figure 3.3. Schematic design and operation of the BOXCARS plates which splits a single laser beam into four parallel beams arranged in the folded BOXCARS configuration. The coating on the plates consists of anti-reflection (AR), 50 % reflection and high reflection (> 99 %) layers.

3.3 Detectors

3.3.1 Photomultiplier tube

A photomultiplier tube (PMT, Hamamatsu, H6780-04) was used as a detector for all LIGS measurements presented in this thesis. It is a device based on the photoelectric effect where absorption of light by the photocathode in the PMT leads to emission of electrons. These electrons pass through several dynodes, where electrons are multiplied by the process of secondary emissions, before resulting in a detectable current signal when reaching the anode. PMTs are extremely sensitive detectors of light, especially in the UV/vis/NIR spectral regions, with the possibility of single-photon detection and ultra-fast response time. However, it is of outmost importance to investigate the operation of the PMT in terms of linearity and saturation point in order to ensure the correctness of the recorded signal. The particular PMT used in this work has a spectral response in the wavelength range of 185-850 nm with a peak sensitivity at 400 nm and a rise time of 0.78 ns. It was connected to an oscilloscope (LeCroy, WaveRunner 6100, 1 GHz) for readout of the signal.

3.3.2 InSb detector

An indium antimonide (InSb) photodiode (Teledyne Judson Technologies, J10D-M204-R04M-60) was used for the DFWM measurements of ammonia. It is cryogenically cooled with liquid nitrogen since it requires a low operating temperature. This type of InSb detector has a round active sensing area of 4 mm in diameter and the signal is amplified by a PA-9 trans-impedance preamplifier in order to maximize the sensitivity, gain and bandwidth. The detector performs well in the 1 to 5.3 µm wavelength region, allowing to record long range excitation scans. As for the PMT, the InSb detector was connected to an oscilloscope (LeCroy, WaveRunner 6100, 1 GHz) for readout of the signal.

3.3.3 Upconversion detector

Even though the InSb detector provides a straightforward usage and operation, it suffers from thermal noise which can affect the detection limit. This is especially an issue when combining weak absorption with low concentration of the targeted molecular species. Instead, during the hydrogen cyanide DFWM measurements, a detection system based on upconversion of the mid-IR laser beam by sum-frequency generation (SFG) with a 1064 nm laser beam [89-92] was utilized. This detection system has the capacity to obtain 500 times better SNR compared to the InSb

detector [90]. A schematic view and a photograph of the upconversion detector are shown in Figure 3.4.

The upconversion system consist of a Nd:YVO_4 crystal being pumped by a 3 W laser diode (880 nm) to produce 1064 nm laser beam which acts as the pump beam. It is guided to the temperature regulated periodically-poled lithium niobate (PPLN) crystal, which is a part of the upconversion laser cavity. The cavity mirrors have a transmissive coating for 880 nm in order to eliminate the residual of the laser diode beam and any fluorescence from the Nd:YVO_4 crystal. Sum frequency-generation occurs in the PPLN crystal between the 1064 nm beam and the incoming mid-IR laser beam to generate a signal beam with wavelength in the visible/near-IR spectral region. The PPLN crystal is designed for SFG of mid-IR wavelengths between 2860-5500 nm. This is covered by having five channels in the crystal with poling periods of 21 µm, 21.5 µm, 22 µm, 22.5 µm and 23 µm. For a fixed crystal temperature, the scanning range is approximately 6 cm^{-1} for a central wavelength near 3 µ while a good conversion efficiency is maintained. The incoming mid-IR laser beam is focused by a lens outside the upconversion detector to have a beam waist diameter of around 180 µm in order to optimally overlap with the 1064 nm beam inside the PPLN crystal. A germanium window prevents transmission (and hence detection) of outside light which has the same wavelength as the upconverted signal beam. The upconverted signal beam is detected by a silicon-based camera (IDS, UI-5240CP-NIR-GL). The 1064 nm beam and the 2nd harmonic (532 nm) generated in the PPLN crystal are prevented from reaching the camera by the long- and shortpass filters placed in front of the camera. The operation of the upconversion detector is summarized in the visual reference [93].

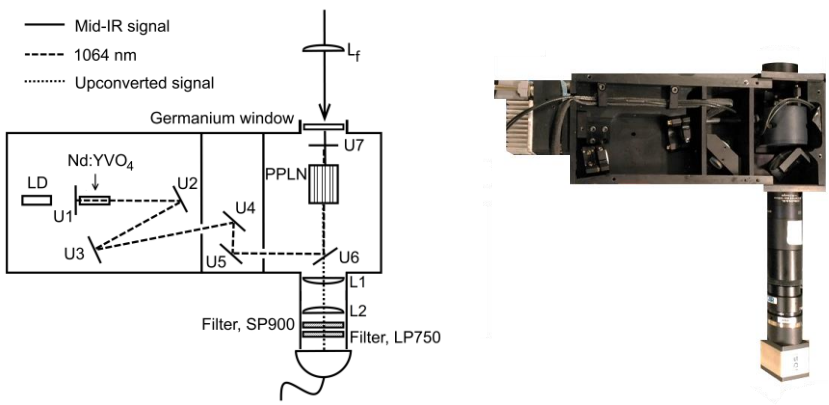

Figure 3.4. A schematic overview (*left*) and an photograph (*right*) of the upconversion detector. The laser diode (LD) pumped Nd:YVO_4 crystal produces 1064 nm laser radiation which is sum frequency mixed with the mid-IR signal beam in the PPLN crystal to generate a near-infrared upconverted signal beam. The abbreviations denote U1-U7: upconversion cavity mirrors, L_f: focusing lens for the mid-IR signal beam, L1-L2: imaging lenses of the upconverted signal onto the camera. Courtesy to R. L. Pedersen [92].

3.4 Burners, heating devices and pressure cell

3.4.1 Porous-plug burners

Two types of porous-plug gas burners were used during the LITGS temperature measurements in flames. At rich flame conditions, flat C_2H_4/air flames were stabilized on a McKenna type burner without the option of having a co-flow. The diameter of the burner is 48 mm and a solid flame stabilizer was positioned 14 mm above the burner surface. Figure 3.5 a) shows a sooty, flat C_2H_4/air flame supported by this porous-plug burner.

A modified Perkin-Elmer burner with a coarser porous plug was used for temperature measurements in lean flames. The burner provided stable flat CH_4/H_2/air flames covering a large flame temperature range. The Perkin-Elmer burner offers the possibility to seed for example liquid salt into the flame. However, this feature was not utilized in the presented work. The burner consists a porous plug with an inner diameter of 25 mm for supporting flat flames that is surrounded by a co-flow region resulting in a total diameter of 45 mm. A solid flame stabilizer was position 20 mm above the burner. Figure 3.5 b) shows the Perkin-Elmer burner. Both burners were supplied with a total flow of around 5 l/min of the fuel/air mixture using mass flow controllers (Bronkhorst).

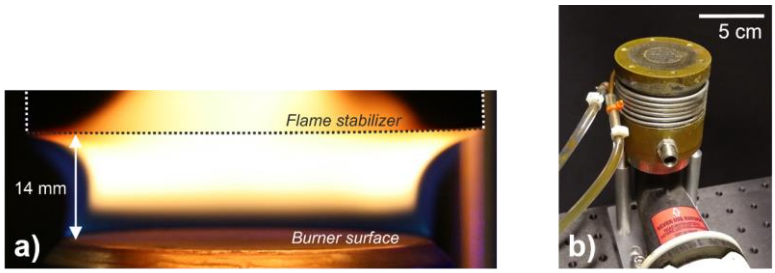

Figure 3.5. a) Sooty premixed flat C_2H_4/air flame stabilized on the porous-plug burner and **b)** a photograph of the modified Perkin-Elmer burner.

3.4.2 Multi-jet burner

The multi-jet burner is a specially designed gas burner [94] which can provide an even and adjustable gas product temperature in order to study the thermochemical conversion of a single biomass pellet. The burner has a rectangular outlet with dimensions 85×47 mm and it consists of 181 individual jets supporting premixed flames, where each and every one is evenly surrounded by a nitrogen co-flow. The operational temperature range of the burner is 1120-1950 K. Figure 3.6 shows the 3D structure and a photograph of the multi-jet burner. The burner was used during

the DFWM measurements where the concentration of hydrogen cyanide was monitored and quantified during the combustion of straw pellets. Premixed flames of $CH_4/H_2/air/N_2$ were supplied to the multi-jet burner in order to create the desired temperature of the hot gas product environment. The straw pellets were positioned on two ceramic rods before being placed in the hot gas environment.

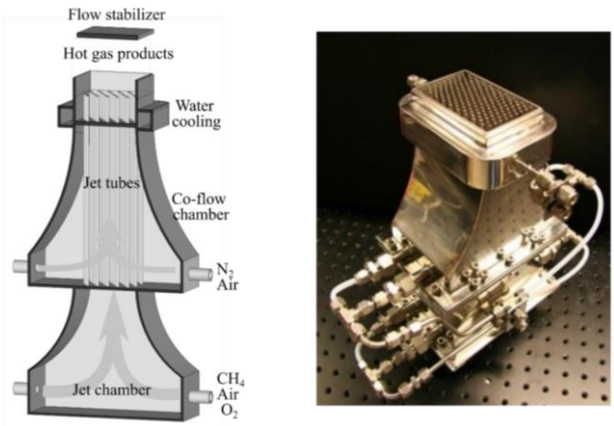

Figure 3.6. A cross sectional 3D structure of the multi-jet burner (*left*) and a photograph of it (*right*). Courtesy to W. Weng [95].

3.4.3 Heating tube

A heating gas tube was used when both DFWM and LIGS experiments were performed in hot gas flows at a controlled temperature. This heating gas tube has an operational temperature range from room temperature up to 820 K. It is an open T-shaped glass tube surrounded by an electric heating wire with insulation material. By driving a controllable and variable current through the wire, the heating gas tube can be heated up to a chosen temperature. The gas is supplied through the bottom of the tube at a typical gas flow of 5 l/min and is heated up as it flows towards the top. The measurements were carried out in the middle of the top T-shaped tube. A calibrated thermocouple of type K was used to measure the gas temperature close to the probe volume and it was inserted from a small opening at the top of the tube. Figure 3.7 shows a photograph of the heating gas tube.

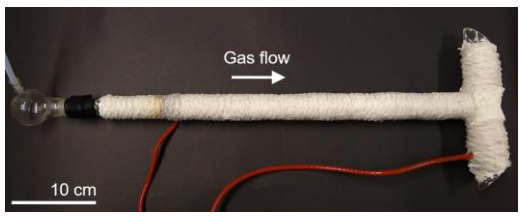

Figure 3.7. Photograph of the heating tube with the indication of the gas flow direction.

3.4.4 Pressure cell

A pressure cell constructed in aluminium with dimensions 80×80×80 mm and a volume of 60 cm^3 was used to investigate the LIGS signals at elevated pressures at room temperature. The cell has three sapphire windows for optical access and is designed to handle pressures up to 12 bar. Figure 3.8 shows a photograph of the pressure cell.

Figure 3.8. Photograph of the pressure cell.

4 Thermometry using LIGS

4.1 Experimental arrangement

A schematic of a typical LIGS experimental arrangement is presented in Figure 4.1, where in this case the dye laser system described in section 3.1.2 is utilized. A mid-IR LITGS experiment can be arranged by employing the complete mid-IR laser system described in section 3.1. The dye laser beam is split into two beams which are the grating formation beams. These pump beams are aligned to fulfil the geometry of the selected crossing angle. A CW probe laser beam is aligned to intersect the laser-induced grating at the Bragg angle and since its wavelength is shorter than the dye laser wavelength, it is aligned between the pump laser beams. All beams are focused by a common lens to intersect in the investigated environment, which is the heated gas flow from the heating tube as illustrated below. It is advantageous to use an alignment mask which indicates and locks the position of all beams both before the focusing lens and after the intersection region. In this way the right crossing and Bragg angles can be maintained. The generated signal is directed towards the detector, which often is a PMT connected to an oscilloscope for signal readout. A trace laser can be aligned to follow the trajectory of the signal beam and thus facilitate the alignment of the detector and corresponding optical components. In this case, a HeNe laser was used as trace laser.

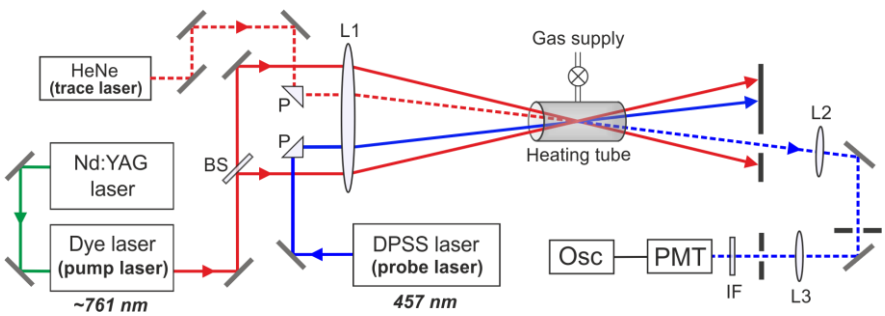

Figure 4.1. Schematic overview of the LIGS experimental setup. This illustration shows the case of LIGS measurements performed in heated gas flows flowing through the heating tube. L1-L3 are fused silica lenses with focal lengths f=1000 mm, f=1000 mm and f=300 mm, respectively. The other abbreviations denote BS: beam splitter, P: fused silica prism, IF: interference filter 457.9 ± 2 nm.

4.2 LIGS in non-combusting environment

A feasibility study has been carried out in order to investigate the potential application of LIGS thermometry on- and off-resonance with the singlet O_2 $\left(b^1\Sigma_g^+\right)$ state at 760 nm. Fundamental investigations of the energy transfer mechanism of this state has been examined under different conditions [61-64]. In this work, two different optical alignment geometries for LIGS were used and a comparison between them was made in order to evaluate the potential application of O_2 LIGS for temperature measurement. The two alignments differed by the choice of the main focusing lens (L1 in Figure 4.1), which had a focal length of 300 and 1000 mm, respectively. The different LIGS parameters are summarized in Table 4.1.

The rotational levels of molecular oxygen are described by the angular momenta *K* and *J*, where *K* represents the rotational angular momentum and *J* is the sum of the rotational (*K*) and spin angular momenta [96-98]. The spectral line notation used here is ${}^{\Delta K}\Delta J(K'')$ where *K''* and *J''* are the quantum numbers of the initial rotational level in the ground state $X\ {}^3\Sigma_g^-(v''=0)$. The resonant LITGS signals were recorded on the ${}^RQ(5)$ absorption line at 761.13 nm, which represents the ${}^RQ$-branch line with *K''* = 5 where $\Delta J = 0$ and $\Delta K = 1$.

The LIGS alignment using the 1000 mm focusing lens was employed for the signals presented in Figure 4.2. The LIGS signals were recorded on the ${}^RQ(5)$ absorption line of O_2 in two different dry gas flows; 9 % O_2 diluted in N_2 and pure N_2, respectively. The Fourier analysis of the signals are presented as insets. The left signal shows the LITGS signal with a contribution from electrostriction. These contributions are observed in the power spectrum where the two peaks indicate the oscillation frequencies due to thermalization (T) and electrostriction (E). The right signal in Figure 4.2 shows a pure LIEGS signal recorded in the N_2 gas flow.

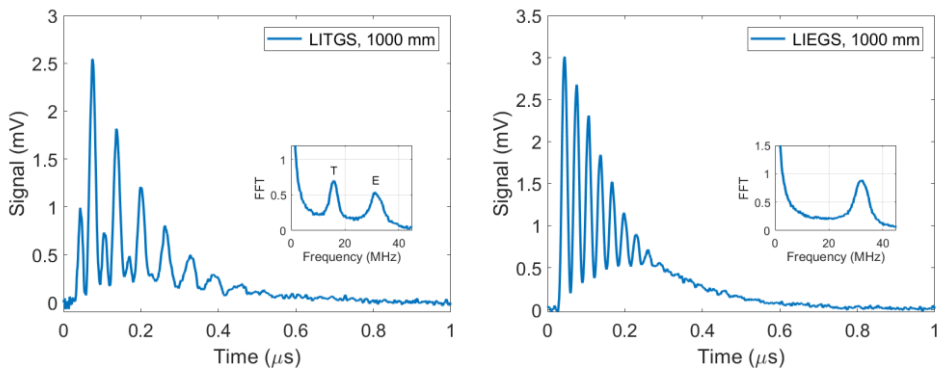

Figure 4.2. LIGS signals using the 1000 mm lens, recorded on resonance with the ${}^RQ(5)$ absorption line of O_2 in a dry gas flow mixture of 9 % O_2 diluted in nitrogen (*left*) and a gas flow of nitrogen (*right*). The Fourier transform of the signals are shown as insets.

Table 4.1. LIGS parameters for the two optical alignments.

Focusing lens (mm)	Crossing angle, θ (deg.)	Grating spacing, Λ (μm)	Oscillation freq. in air, f_{osc} (MHz)	Bragg angle, θ_B (deg.)
300	3.7	11.8	29.2	1.1
1000	1.9	22.8	15.1	0.57

Figure 4.3 shows the LIGS signals obtained when using the alignment with the 300 mm focusing lens. Both signals were recorded in room air, where the left signal was on resonance with the ${}^{R}Q(5)$ absorption line of O_2 and thus creating a thermal grating. The inset shows the Fourier analysis of the signal where oscillation frequencies originating from thermalization (T) electrostriction (E) can be identified. Normally a peak should be observed instead of a dip at the frequency from thermal signal. This could be due to its low signal contribution to the overall LIGS signal. The right signal shows the LIEGS signal recorded at 761.18 nm. Overall, the signal intensities are higher for this alignment and the relative contribution from the thermal grating to the LIGS signal is lower than the case in Figure 4.2, indicating a more rapid increase of the electrostrictive grating with higher pump laser power density.

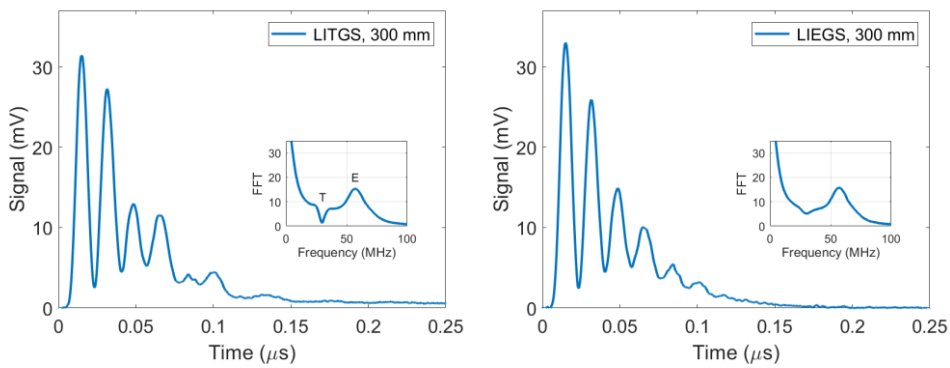

Figure 4.3. LIGS signals using the 300 mm lens, recorded in room air on-resonance with the ${}^{R}Q(5)$ absorption line of O_2 (*left*) and off-resonance at 761.18 nm (*right*).The Fourier transform of the signals reveal the oscillation frequency and are shown as insets.

Figure 4.4 shows the power dependence of the LIGS signals performed for both alignments. The LITGS and LIEGS signals were easier to distinguish for the 1000 mm alignment as seen in Figure 4.2. However, for the alignment using the 300 mm focusing lens, the electrostrictive contribution dominated the signal, even when the laser wavelength was resonantly tuned to an oxygen absorption line. This resulted in an impossible separation between the electrostrictive and thermal signal

contributions and hence the power dependence was only performed for LIEGS signals. These results indicate that the optical arrangement using the 300 mm focusing lens produces stronger LIEGS signals and would be beneficial to use for temperature measurements in practical applications, especially at elevated pressures.

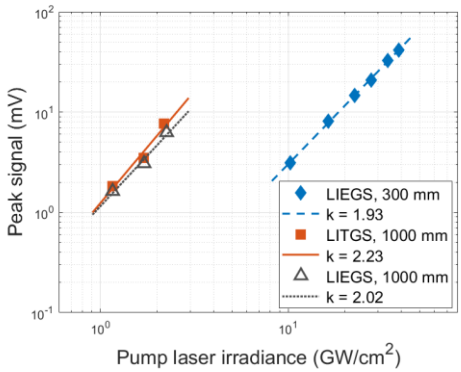

Figure 4.4. Signal dependence upon the pump laser irradiance for LIEGS and LITGS signals recorded using the two optical alignments. The LIEGS signals with 300 mm (blue) were recorded off resonance in room air while the LITGS and LIEGS signals with 1000 mm (red, purple) were recorded on the ${}^{R}Q(5)$ line in dry gas flow of 9 % O_2 in N_2 and solely N_2, respectively.

Even though the pulse energy of the pump laser was the same during the measurements when the signals in Figure 4.2 and 4.3 were recorded (50 mJ/pulse), the pump laser irradiance was higher for the alignment with tighter focus (300 mm focusing lens), which lead to generation of strong laser-induced electrostrictive gratings and 5 times stronger signals. The LIGS signal at elevated temperatures is expected to decrease in intensity, due to lower density in the probe volume and thus weaker grating. Therefore, the LIGS alignment with the tighter focus (300 mm focusing lens) is more suitable for temperature measurements and the following discussion concerns only this alignment.

Figure 4.5 shows the off-resonance, normalized LIEGS signals recorded at different temperatures in heated gas flows of dry air using the heating tube described in section 3.4.3. The inset shows the Fourier transform of the signals. The measurements were performed at atmospheric pressure and the LIEGS signals were recorded at 762.4 nm. As it can be observed, the signals decay faster with increasing temperature since the acoustic waves travel faster out of the probe volume due to the shorter acoustic transit time with increasing speed of sound (see Eq. 2.22). The signal at 700 K contains only three oscillations, which makes it difficult to determine the oscillation frequency since the frequency peak in the power spectrum is wider and on a background slope.

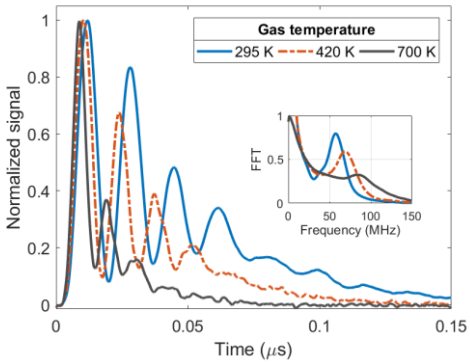

Figure 4.5. Normalized LIEGS signals at different temperatures in a dry air gas flow at atmospheric pressure. The measurements were performed using the LIGS alignment with the 300 mm fousing lens. The inset shows the corresponding Fourier transform of the signals.

Table 4.2 shows the LIGS temperature retrieved both from direct frequency analysis in the power spectrum and from fitting a simulation model to the signal as described section 2.3.3, where only the electrostrictive part has been considered for the LIEGS signals, in order to extract the oscillation frequency. The presented averaged values are based on 100 single-shot signals where the standard deviation of these indicate the precision of the technique. The Fourier transform analysis is straight forward to use but becomes problematic when the quality of the signals is poor, which is often the case at elevated temperatures. The fitting of a simulation to the signal is more demanding but provides lower uncertainties in the oscillation frequency determination. As indicated from the results at the gas temperature 700 K, both methods have poor precision which was due to the poor signal quality in terms of intensity, noise level and few oscillation peaks to base the oscillation frequency determination on. It was observed that 700 K was the upper limit of the LIEGS technique with the present setup.

Table 4.2. The average single-shot LIEGS temperature at each gas temperature measured with thermocouple (type K), determined using the Fourier transform method or the fit simulation method. The precision in each value is given by the standard deviation of the temperature derived from 100 single-shots.

Analysis method	**295 K**	**420 K**	**700 K**
Fourier transform	295 ± 7 K	436 ± 26 K	732 ± 90 K
Fit simulations	295 ± 4 K	446 ± 13 K	708 ± 70 K

Furthermore, LIGS signals in dry air at different pressures were investigated at room temperature. These measurements were performed at 1-7 bar in the pressurized cell as described in section 3.4.4, using the LIGS alignment with the 300 mm focusing

lens. Figure 4.6 shows the resonant LITGS signals recorded on the ${}^{R}Q(5)$ line and the non-resonant LIEGS signals recorded at 762.4 nm. The inset shows the main oscillating part of the LITGS signals. At 1 bar the thermal part of the signal is very weak and the electrostrictive part is dominant. With increasing pressure, the thermal contribution of the signal grows and it can be seen as the oscillation peaks with even number gets higher intensity compared to the odd number peaks. The initial rise of the long tail in the signals at higher pressures occur due to a slow energy transfer mechanism, that gains more intensity as the pressure increases [61]. The decay of the signal tail depends on the thermal diffusivity of the gas. Measuring the decay of the signal can be used for pressure measurements [58]. The off-resonant LIEGS signals on the other hand remain almost identical at increasing pressures. The reason is that LIEGS signals are not affected by collisions and thermal diffusion, but rather on the decay of the acoustic waves which are affected by the acoustic damping and acoustic transit time, as described in Eqs. 2.21 and 2.22. The intensity of the signals in Figure 4.6 are normalized to the first peak in order to be able to visualize all signals on the same scale. The intensity of the signals was observed to increase up to 45 times when increasing the pressure from 1 bar to 7 bar.

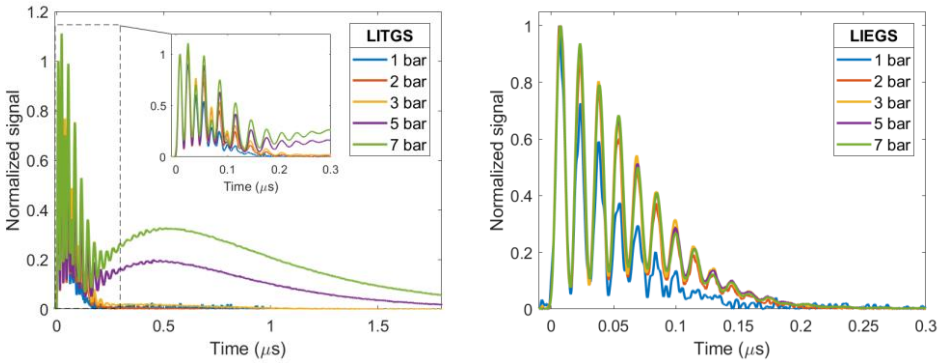

Figure 4.6. LIGS measurements performed in dry air at room temperature and different pressures. LITGS signals recorded on the ${}^{R}Q(5)$ line at different pressures, where the inset shows a zoom on the first oscillating part of the signal (*left*). The non-resonant (LIEG) signal was recorded at 762.4 nm at different pressures (*right*). The signal intensity has been normalized to the first peak.

The results from this feasibility study have shown the potential of application of LIGS around 760 nm using the tighter focus (300 mm focusing lens) for temperature measurements. At elevated pressures, the measurements can be carried out both on- and off-resonance with O_2 $\left(b^1\Sigma_g^+\right)$. The thermal and electrostrictive contributions to the LIGS signal when probing an oxygen transition opens up the possibility of performing local concentration measurements as described in [59, 99]. However, considerations regarding the damage threshold of the windows on the high-pressure chambers and engines, as well as any beam steering effects must be investigated prior measurements.

4.3 Flame temperature measurements

Mid-infrared laser diagnostics offers the possibility to study and utilize the fundamental ro-vibrational transitions of several combustion-related species, such as water, carbon dioxide and hydrocarbons. Here, the focus is to utilize water absorption in the product zone of premixed flames to investigate the feasibility of performing temperature measurements in flames with mid-IR LITGS. Besides measuring temperature, characteristics such as signal strength and robustness of the technique was examined. Resonant absorption of water was performed by tuning the pump laser wavelength to the hot water absorption lines at 3231 cm^{-1}. All measurements were performed in premixed laminar flames at atmospheric pressure with different equivalence[2] ratio. In contrast to the work presented in section 4.2, no electrostrictive signal was observed here. The probe volume was around $0.5\times0.5\times16$ mm^3. This work is described in more detail in Paper I and II.

4.3.1 Thermometry using mid-IR LITGS

Water is one of the global products from combustion which has strong absorption in the mid-IR spectral region. Therefore, the feasibility of mid-IR LITGS based on water absorption was investigated for thermometry, in terms of precision and accuracy of the technique. The measurements were performed in the product zone of eight laminar premixed CH_4/H_2/air flames with equivalence ratio ranging between $0.6\leq \varphi \leq 1.05$. These flames provided a temperature range of approximately 350 K. The measurements were performed by probing the hot water lines at 3231 cm^{-1}. During these measurements the crossing angle between the pump beams was 2.8°, resulting in a grating spacing of around 63 µm. To obtain the temperature in the probe volume, laser Rayleigh scattering (LRS) measurements were performed using the CW DPSS laser. A program called CEA (Chemical Equilibrium with Applications [100]) was then used to simulate the gas composition of the investigated flames at the temperatures retrieved from the LRS measurements.

Figure 4.7 shows a single-shot LITGS signal of water recorded in a stoichiometric CH_4/air flame. In order to precisely extract the oscillation frequency used for temperature calculations (see section 2.3.2), a simulation model as described in section 2.3.3 was fitted to the signal. The model contained an instantaneous part (I_i), and two finite energy transfer parts; fast (I_{f1}) and slow (I_{f2}) energy transfer. The

[2] Equivalence ratio is a useful characterizing parameter of the mixture level between fuel and oxidizer in a premixed flame. It is defined as $\varphi = \left(n_{fuel}/n_{oxidizer}\right)/\left(n_{fuel}/n_{oxidizer}\right)_{st}$ where n is the number of moles and the suffix stands for stoichiometric conditions. When $\varphi = 1$, the mixture is referred to as stoichiometric, while $\varphi < 1$ is fuel-lean condition and $\varphi > 1$ is fuel-rich condition.

simulation parameters for the signal in Figure 4.7 are presented in Table 4.3. The single-shot precision of the technique is based on the normal distribution of the oscillation frequency obtained from 100 single-shot signals, which resulted in a temperature precision better than 1 % of the LITGS retrieved flame temperature for each flame. This can be compared with the well-established diagnostic technique CARS used for temperature measurements, where a precision of 1-1.5 % is commonly obtained [101-103].

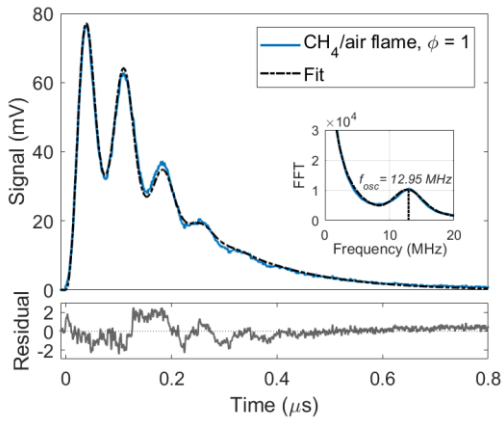

Figure 4.7. Single-shot mid-IR LITGS signal of water recorded in the product zone of a stoichiometric CH_4/air flame. From the simulation fit the precise oscillation frequency can be obtained (inset) for temperature calculation. The simulation parameters are presented in Table 4.3.

Table 4.3. Simulation parameters used for the signal in Figure 4.x. The model consist of $I(t) \cong \left(I_i(t)+I_{f1}(t)+I_{f2}(t)\right)^2$. See section 2.3.3 for details.

$M_i/M_{f1}/M_{f2}$	τ_{th} (µs)	τ_{tr} (µs)	τ_{f1} (µs)	τ_{f1} (µs)	f_{osc} (MHz)
-0.0086/0.66/-0.33	0.425	0.147	0.0508	0.135	12.95

Figure 4.8 shows both the mid-IR LITGS and LRS temperature for the eight flames. The LITGS temperature in each flame is an average of the temperature derived from 100 single-shot mid-IR LITGS signals of water. The calculated temperatures are lower compared to the adiabatic flame temperature since the measurements were performed in the product zone of the flame. There is a good agreement in the temperature measurements between the two techniques where the small difference could arise from a difference in the exact position above the burner where the measurements were performed.

The main source of uncertainty in the mid-IR LITGS temperature arises from the uncertainty in the gas constants γ/M_{gas}, which is estimated to be ± 2 %, and the uncertainty in determining the grating spacing Λ, (around ± 1 µm). This results in

an overall accuracy of 2.5 % in the mid-IR LITGS temperature measurement and is reflected as error bars in Figure 4.8. This can be compared with the typical accuracy for fs/ps rot-CARS being 3-5% [101] and for fs/ps vib-CARS is 3.3% [102].

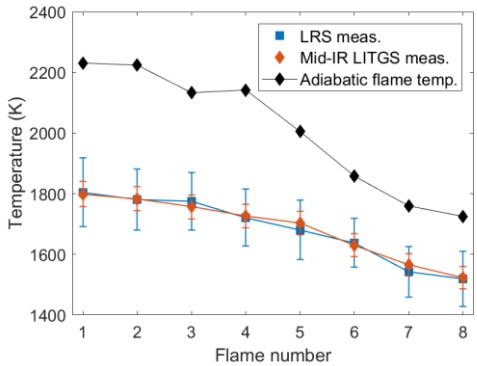

Figure 4.8. Flame temperatures at 8 mm above the burner in flames 1-8, measured with laser Rayleigh scattering (LRS, blue) and mid-IR LITGS (red). The adiabatic flame temperature of the different flames is included for comparison.

Mid-IR LITGS was also applied for thermometry in sooty C_2H_4/air flames by probing the hot water line at 3231 cm^{-1}. During these measurements the crossing angle between the pump beams was 5.65°, resulting in a thermal LIG with a grating spacing of around 31 µm. Figure 4.9 shows the LITGS signal of water in the product zone of a C_2H_4/air flame with φ=2.57. This LITGS alignment had a tighter focus of the pump beams compared to the measurements above, resulting in a two times narrower width of the grating and hence two times faster acoustic transit time (see Eq. 2.22). The exponential decay of the signal due to thermal diffusion is four times faster according to Eq. 2.23 because of the half grating spacing. A two-colour four-wave mixing (TC-FWM) signal was observed to appear in the LITGS signal when measurements were performed further downstream in the product zone, see Figure 4.9. This kind of signal has been previously observed in sooty flames [104] and it appeared simultaneously with the pump laser pulse. The TC-FWM signal is proposed to originate from either present or formed carbon, C_2, since the probe laser wavelength (457 nm) is resonant with one weak C_2 transition.

Furthermore, the change in gas constants, γ/M_{gas}, was observed to be minimal for fuel-lean or stoichiometric flames when the equivalence ratio was varied. However, for fuel-rich flames the gas constants were found to vary significantly with the gas composition. The calculation of the speed of sound, and thus temperature, was most affected by the estimation of the hydrogen (H_2) concentration present in the probe volume.

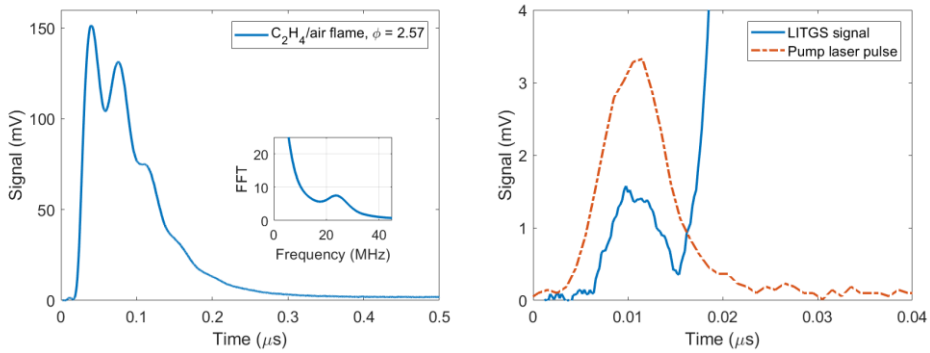

Figure 4.9. LITGS signal of water in a C_2H_4/air flame with φ=2.57 (*left*), recorded at 10.5 mm above the burner surface in the flame shown in Figure 3.5 a). The inset shows the Fourier transform of the signal, revealing an oscillation frequency of around 24 MHz. A zoom-in of the LITGS signal shows the C_2 signal occuring simultaneously with the pump laser pulse (*right*).

4.3.2 Excitation spectrum

Laser-induced thermal grating spectroscopy (LITGS) relies on efficient collisional quenching of the probed molecular transition in order to form a thermal grating, where the molecular energy (electronic, vibrational or rotational) is deposited into the bulk gas as kinetic energy, i.e. heat. Not all molecular transitions result in a LITGS signal, a property which was observed for water in this work.

Figure 4.10. shows the mid-IR LITGS excitation spectrum recorded in the product zone of a CH_4/H_2/air flame with φ=0.6. The spectrum was obtained by scanning the pump laser wavelength across 3225-3260 cm^{-1} while recording the integrated LITGS signal at each scanning point. The black curve shows a simulation of the absorption coefficient (σ) of water at 1800 K, based on the data from HITEMP 2010 [44] and is included for qualitative comparison. Comparing these two spectra, it is observed that there are several LITGS lines missing and that the shape and intensity is different for the present LITGS lines. The left inset in Figure 4.10 shows the group of the temperature sensitive hot water lines between 3230-3231.5 cm^{-1}, where the third line is missing. The right inset shows additional missing water LITGS lines between 3257.6-3258.5 cm^{-1}.

The rotational energy levels of water are characterized by the quantum numbers J, K_a and K_c, where J represents the total angular momentum and K_a and K_c are projections of J on the axes of inertia [44]. By investigating the energy level data available in HITEMP 2010 for the transitions with negligible or non-existing LITGS lines, it became clear that these transitions have a high Einstein A-coefficient, which is describing spontaneous emission, and that the difference in quantum number K_a between the ground state and excited state is zero, $\Delta K_a = 0$. On the other hand, the

strong LITGS lines was found to consist of transitions with ΔK_a = -1. It is clear from the analysis of the spectrum that for mid-IR LITGS thermometry using water absorption, it is important to probe the right water line ($\Delta K_a \neq 0$) in order to generate a strong LITGS signal.

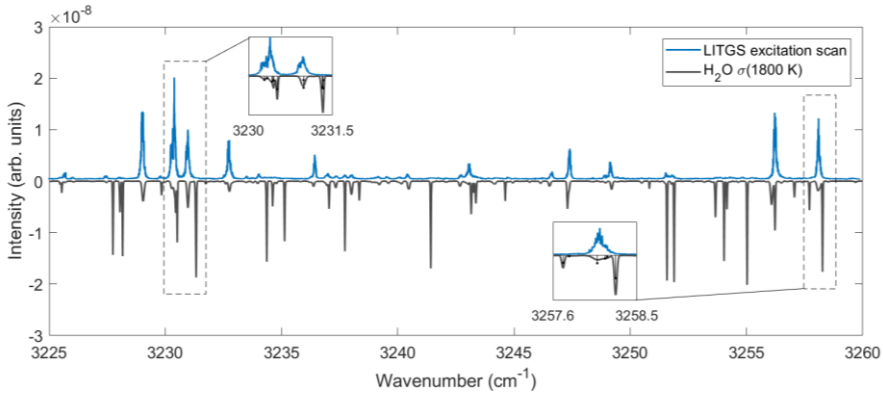

Figure 4.10. Mid-IR LITGS excitation scan in a CH_4/H_2/air flame with φ=0.6. Simulation of the absorption coefficient for water at 1800 K is included for qualitative comparison. Two observations can be made; (1) few spectral lines associated with water are not present in the LITGS excitation scan and (2) the LITGS lines are different both in terms of shape and intensity.

4.3.3 Additional observations

The use of a mid-IR laser as pump beams in a LITGS experiment provides the possibility of having larger grating spacing than arranged before in the UV or visible spectral regions. Depending on the crossing angle, typical values of the grating spacing used in the mid-IR are in the range of ~30-65 µm. This raised the question if the probe laser beam could be aligned in multiples (m) of the Bragg angle as $\theta_m = m\theta_B$ and the possible application of it. The Bragg diffracted signal beam has then the same angle as the incident probe beam.

Figure 4.11 shows the LITGS signals of C_2H_2 recorded at 3230.68 cm^{-1}, where the probe laser beam (457 nm) is aligned to intersect the grating at $\theta_1 = \theta_B$, $\theta_2 = 2\theta_B$ and $\theta_3 = 3\theta_B$. Also shown in Figure 4.11 is the Fourier transform of each signal where the oscillation frequency can be identified. These measurements were performed at atmospheric conditions in a gas flow mixture containing C_2H_2 diluted in N_2. The alignment of the pump beams was the same for all Bragg angle measurements, with a grating spacing of 63 µm. The concentration of C_2H_2 was adjusted in order to obtain strong LITGS signals for all investigated Bragg angles. Despite the substantial increase in C_2H_2 concentration, the LITGS signal intensity decreased due to the decrease in Bragg diffraction efficiency. The different parameters regarding the Bragg angle alignments are summarized in Table 4.4.

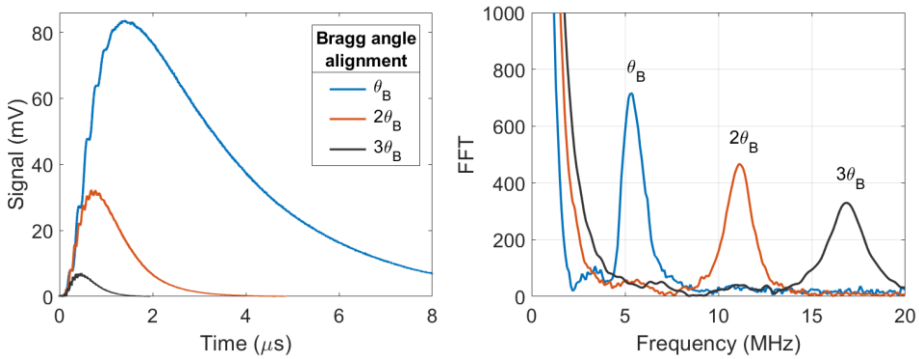

Figure 4.11. LITGS signals of C_2H_2 using different Bragg angle alignments of the probe laser (*left*) and the Fourier transform of each signal indicates the oscillation frequency (*right*). (*Unpublished results.*)

The signal from the probe laser alignment at the first Bragg angle has an oscillation frequency of 5.4 MHz, which is correlated to the frequency determined by Eqs. 2.4 and 2.18. However, for the LITGS signals where the probe laser is aligned at the 2nd and 3rd Bragg angle, the oscillation frequencies are two and three times higher than the ordinary oscillation frequency, respectively. Here, the crossing angle between the pump beams did not change and therefore the grating spacing of the stationary laser-induced thermal grating is the same for all cases. However, still a higher frequency is detected. In addition, the exponential decay of the signal due to thermal diffusion increases with the multiple of Bragg angle alignment, which could imply that a grating with smaller grating spacing is probed.

Table 4.4. Parameters for the different multiples of Bragg angle alignment.

Multiple	Bragg angle (deg.)	Osc. frequency (MHz)	C_2H_2 concentration (%)
1	0.2	5.4	0.04
2	0.4	11.0	0.2
3	0.6	16.8	1.1

Stevens [105] presented in his doctoral thesis the occurrence of higher harmonics of the oscillation frequency in the power spectrum from a LITGS signal of NO_2 diluted in nitrogen and recorded at 40 bar. In that work, the probe laser was aligned to intersect the laser-induced thermal grating at the first Bragg angle. This finding was addressed to originate from saturation of the molecular absorption which could cause a “nonlinear conversion of laser intensity to heat in the thermal grating”. It

would then lead to formation of a non-sinusoidal grating where the heat maxima are flattened and the thermal grating has a shape of a square wave. A consequence of this is no complete destructive interference of the acoustic waves and a perturbation of density, which would add a contribution to the grating signal.

In our case the pump laser energy was around 7 mJ/pulse, which indicated slight saturation. Here, only the ordinary oscillation frequency was observed in the frequency analysis of the LITGS signal from the first Bragg angle alignment. Detection of higher harmonics of the oscillation frequency seems to be coupled with the selected Bragg angle alignment of the probe beam. A possible application of this alignment approach of the probe laser would be when it is experimentally difficult to align and obtain a clean signal without spatial overlap and interference from the probe laser beam.

As an example of mid-IR LITGS, Figure 4.12 shows the LITGS signal of water recorded at 3231 cm^{-1} in the product gases from a stoichiometric CH_4/air flame. The signal is an average of 200 shots. The crossing angle of the pump laser beams was 1.4°, resulting in a grating spacing of around 126 µm. The probe laser was aligned to intersect the grating at the second multiple of Bragg angle, 0.2°. An oscillation frequency of around 12.7 MHz is detected, which corresponds to the frequency from alignment with a grating spacing of 63 µm and ordinary Bragg angle of the probe laser, see Figure 4.7. The signal strength with a signal-to-noise better than 1800 and a long signal duration, even in atmospheric flames where thermal diffusion is high, indicate the possibility for application of this alignment strategy. The signal was non-detectable when the probe laser beam was aligned to intersect the laser-induced grating with grating spacing of 126 µm in the third multiple of Bragg angle.

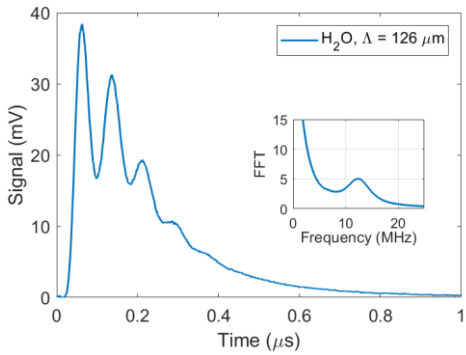

Figure 4.12. LITGS signal of water recorded in a CH_4/air flame with φ=1 at 3231 cm^{-1} with a grating spacing of 126 µm. The inset shows the power spectrum where the oscillation frequency is identified. (*Unpublished results.*)

5 Concentration measurements using DFWM

5.1 Experimental arrangement

A schematic of a typical mid-IR DFWM experimental arrangement is shown in Figure 5.1, where the mid-IR laser system has been described in Chapter 3. The laser beam is split into four beams of approximately equal intensities using the BOXCARS plates. Three of these beams are crossed by a focusing lens (noted as L3), while the fourth beam acts an alignment beam since the generated signal follows its trajectory. The intensity of the fourth beam is reduced during alignment by utilizing a set of neutral density filters with sufficient damping in order to avoid saturation of the detector. However, this beam is blocked during the measurements. The crossing occurs in the investigated gaseous environment and the generated signal was detected either by the InSb detector or the upconversion detector. The probe volume depends on the focal length of the selected focusing lens L3, but is commonly around 0.4×0.4×6 mm^3.

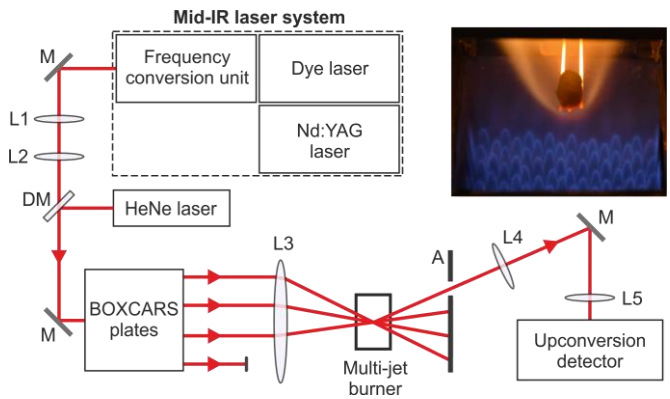

Figure 5.1. Schematic overview of the mid-IR DFWM experimental setup. L1-L5 are CaF_2 lenses with the following focal lengths f=500 mm, f=-200 mm, f=500 mm, f=500 mm and f=100 mm, respectively. The other abbreviations denote M: gold mirror, DM: dichroic mirror, A: aperture. The photograph shows an angled top view of the multi-jet burner with gasification of a straw pellet.

The arrangement depicted in Figure 5.1 shows the mid-IR DFWM measurements where the hydrogen cyanide (HCN) released from gasification of a straw pellet was detected. The crossing point was above the pellet and the upconversion detector was used for sensitive detection of HCN. The photograph shows the burning straw pellet above the multi-jet burner in a tilted top view. Two ceramic rods are holding the pellet and individual jet flames of the multi-jet burner can be seen.

5.2 Hydrogen cyanide released from straw pellet combustion

Hydrogen cyanide is a key molecular species in the nitrogen chemistry of thermochemical conversion of biomass, where the relation between ammonia and HCN released from biomass combustion depends on the conversion temperature [106, 107]. In this work, mid-IR DFWM was utilized to detect and quantify the HCN concentration released from gasification of straw pellets. For this purpose, the multi-jet burner was used and the measurement point was located 3 mm above the straw pellets. The upconversion detector was utilized during these measurements, which were performed during the devolatilization[3] stage since most detectable amount of HCN was released then. Thermochemical conversion of biomass pellets is a time-varying process and it is therefore necessary to perform these measurements by tuning the laser wavelength on the absorption line rather than scanning across the line. The selected interference-free absorption line of HCN is P(20), which is located at 3248.48 cm^{-1} in the v_1 vibrational band. This work is presented in more detail in Paper V.

In order to perform quantitative measurements, both the concentration and temperature dependence of the DFWM signal from the P(20) line of HCN was determined. The relation obtained from those investigations were used to translate the DFWM signal intensity to HCN concentration. Furthermore, the temperature information above the pellet during the devolatilization stage was required to be known and for this purpose the thermometry method suggested by Sun *et al.* [29] was applied.

This thermometry method utilizes two group of temperature sensitive hot water lines at 3230-3231.5 cm^{-1}. The intensity of the two groups changes dramatically within the temperature range of 1000-2000 K and results in a temperature dependent ratio which can be used as a calibration curve for temperature. A simulation of the mid-IR DFWM spectrum of the water lines is shown as inset in Figure 5.2 for two

[3] Devolatilization stage is considered to be when most volatiles are released of formed from thermochemical conversion of biomass and it is followed by the char stage.

different temperatures, 1200 K and 1800 K. The two water line groups are indicated as A and B, respectively.

Since the signal during the devolatilization stage of the straw pellet vary with time, the laser wavelength was kept constant at the peak of the each of the two water line groups during measurements. The mid-IR DFWM water signal from 10 consecutive pellet measurements was recorded and averaged for each group. The ratio was then obtained for the averaged DFWM water signals to determine the temperature in the measurement volume. Figure 5.2 shows the obtained temperature above the straw pellet during the devolatilization stage for the three investigated gasification environment temperatures. The steep drop in temperature at the beginning is when the pellet is inserted above the multi-jet burner. This follows by the devolatilization stage where release or formation of numerous different chemical compounds occur as well as drying of the pellet. The increase in temperature towards the end reflects the end of the devolatilization stage where most volatile compounds were released and a dry pellet is left.

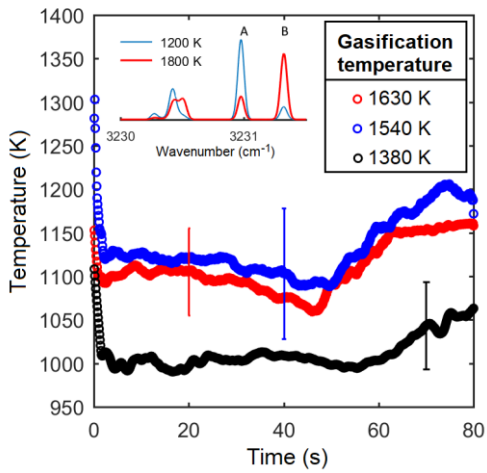

Figure 5.2. The retrieved temperature 3 mm above the straw pellet during the devolatilization stage at three different gasification conditions. The inset shows the simulated mid-IR DFWM spectrum of the temperature sensitive water line groups at 3230-3231.5 cm^{-1}. The temperature was retrieved according to the method presented in [29] where the peak ratio between the water line groups A and B was taken during the whole devolatilization stage. Ten measurements were taken for each water line group and the graphs is an average of the 10 temperature measurements. The error bars indicate the average standard error, which is obtained to be ± 50 K for gasification cases 1630 K and 1380 K, and ± 75 K for case 1540 K

The HCN signal is quantified according to the description in section 2.2.3. Figure 5.3 shows the quantified HCN release history during the devolatilization stage from gasification of a single straw pellet under the gasification environment temperature of 1540 K. In contrast to flames based on a continuous gas flow of fuel, the biomass

pellets exhibit a large natural variation in composition. Therefore, a number of independent measurements need to be performed in order to obtain a statistically significant average value with an acceptable uncertainty. For this work 15 independent pellet measurements were required and an average HCN release history is shown in Figure 5.3 as the red curve. The photographs show different stages of the measurement period, where preheating of the pellet occurs until ~15 s after the pellet has been inserted in the gasification environment above the multi-jet burner. Thereafter, the release of HCN increased significantly and reached its peak at around 1500 ppm at roughly 40 s, when a sooty volatile flame was formed. This followed by a gradual decline in the HCN release until it was close to the value below the detection limit as no volatile gas was released from the pellet, indicating the start of the char gasification stage (80 s) and thus end of the devolatilization stage. A repeatable scattering event occurred at 60 s during most pellet measurements at this gasification temperature, where numerous large particles were released. The maximum HCN concentration released during the other two gasification temperatures, 1380 K and 1630 K, is around 750 ppm and 1500 ppm, respectively. These results are consistent with existing literature [106, 108, 109].

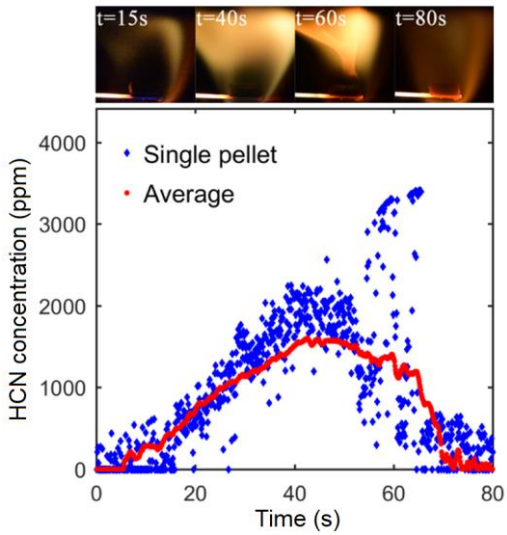

Figure 5.3. Recorded HCN release during the devolatilization stage from gasification of a single straw pellet at the gasification environment temperature 1540 K. The red curve is an average of 15 independent measurements. The meaurement was performed on the P(20) line of HCN. The photographs show the different stages of the measurement period.

The major benefit of utilizing the group of hot water lines for thermometry is that it enables the use of same experimental arrangement where the conditions are kept the same for the calibration, temperature and concentration measurements. Furthermore, the hot water lines are spectrally close to the P(20) line of HCN, hence

a fast and small change in laser wavelength is required between the set of measurements.

However, the main source of uncertainty in the derived HCN concentration arises from the temperature measurements above the pellet. The method relies on the accuracy of tuning the laser to the center of the peak of each water line group, between each measurement. Inaccuracies in the spectral position of the laser line can result in systematic errors. A better approach would be to scan across the water lines to obtain the peak ratio. However, this was not a possible approach during these time-varying pellet measurements. Thermometry using LIGS could be an alternative for future work, given that a there is a good, or at least a decent, estimation of the gas composition.

5.3 Ammonia detection at elevated temperatures

Ammonia is a molecular species of interest both as a fuel itself and during the thermochemical conversion of biomass since, along with HCN and isocyanic acid (HCNO), it is an important precursor of NO_x [106, 108]. Therefore, it is essential in the nitrogen chemistry of thermochemical conversion of biomass to investigate its production rate and mole fraction. In this work, mid-IR DFWM was employed to investigate the feasibility of the technique for detection of ammonia at 2.3 µm using the InSb detector. The spectrum of NH_3 in this wavelength region consists mainly of the combinational bands $\nu_2 + \nu_3$ and $\nu_1 + \nu_2$, meaning that the vibrational energy is associated to combination of several vibrational motions of the molecule. It is beneficial for spectroscopic measurements due to low or negligible interference from water, which otherwise can be problematic for diagnostic applications in flames. This investigation is described in more detail in Paper VI.

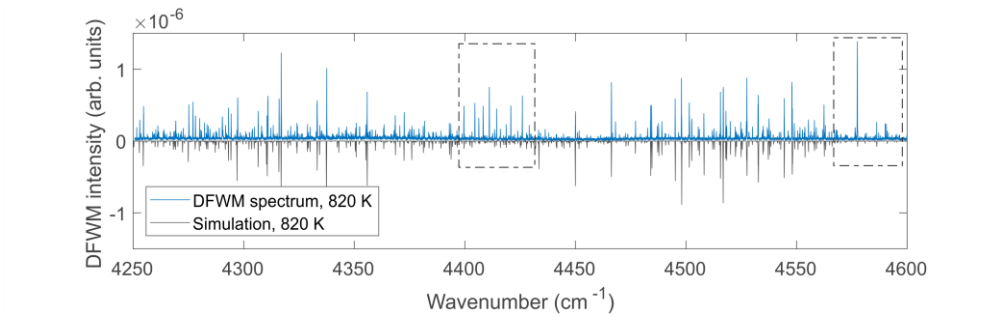

Figure 5.4. Mid-IR DFWM spectrum of ammonia recorded at 820 K in a gas flow mixture of NH_3/N_2. The concentration of ammonia is 2.93 %. A simulation of the DFWM spectrum at the same temperature is included for identification of the spectral lines and it based on the on the data from HITRAN database [110]. The dashed boxes indicate spectral regions where the simulation data is incomplete.

Figure 5.4 shows the mid-IR DFWM spectrum recorded in a heated gas flow mixture containing 2.93 % ammonia in nitrogen. The excitation scan was performed at 820 K and a simulation of the DFWM spectrum (see section 2.2.3) at the same temperature is shown for qualitative comparison in order to identify the spectral lines. The simulation is based on the data from the HITRAN database [110] and in some regions it is incomplete or insufficient, as indicated by the dashed boxed in Figure 5.4.

Detection of ammonia was performed by probing the strongest ro-vibrational transition and investigating the concentration dependence of the DFWM signal at a few selected gas temperatures. Figure 5.5 shows the concentration dependence of ammonia acquired at 296 K by scanning over the $^{R}R_3(3)a$ line at 4484.1 cm^{-1} in the $\nu_2 + \nu_3$ band and integrating the DFWM signal. Each measurement data point is an average value from five consecutive scans, and the error bars indicate the standard deviation of these results. The concentration dependence of the DFWM signal follows a quadric relation, which is expected since the signal is quadratically proportional to the number density as expressed in section 2.2.1.

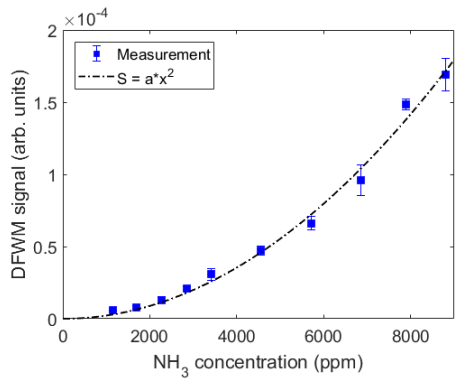

Figure 5.5. Concentration dependence of the ammonia mid-IR DFWM signal acquired at 296 K. The measurement data points are reflecting an average value of the line-integrated DFWM signal after performing five consecutive scans over the $^{R}R_3(3)a$ line in the $\nu_2 + \nu_3$ band, where the error bars show the standard deviation of these results. As expected, the measurements follow a quadratic relation as expressed in section 2.2.1.

From the concentration dependence measurements, the detection limit of the technique can be estimated. This was done by extrapolating the fitted quadratic curve to a value where the signal-to-noise ratio is equal to 1. The estimated detection limits of ammonia at different temperatures using mid-IR DFWM are presented in Table 5.1. The main limitation in the detection limit of the technique stems from the low absorption cross section of the ammonia lines in this spectral region.

The release or formation of NH_3 during thermochemical conversion of biomass pellets occur mainly during the devolatilization stage, where the ammonia

concentration is around 1000 ppm [106, 109]. For these low concentrations, the detection of ammonia around 2.3 μm using mid-IR DFWM cannot be applied for sensitive ammonia detection from biomass pellets.

Table 5.1. Estimated detection limit of NH_3 at different gas temperatures using mid-IR DFWM. The measurements were performed in heated gas flows mixtures of ammonia diluted in N_2 at atmospheric pressure.

Temperature (K)	Detection limit (ppm)	Detection limit (molecules/cm^3)
296	550	1.4×10^{16}
550	3700	4.9×10^{16}
820	7900	7.1×10^{16}

A possible improvement of the detection limit could be achieved by utilizing the upconversion detector equipped with a PPLN crystal designed for this mid-IR wavelength region. Another approach would be to probe the slightly stronger absorbing fundamental vibrational band ν_1 at 3337 cm^{-1} (3 μm) of ammonia in combination of the use of the upconversion detector. However, the main concern in that spectral region is the broad spectral overlap with water and therefore a careful selection of the NH_3 absorption line must be made.

6 Conclusions and outlook

The aim of the work presented in this thesis has been to further develop the infrared laser-induced grating techniques for quantitative measurements in reactive flows, such as flames. The overall focus has been to investigate the applicability and robustness of infrared LIGS for temperature measurements in terms of signal strength, precision and accuracy of the technique. In addition to that, mid-IR DFWM has been investigated and applied for concentration measurements. The result of this work opens up for future application of these techniques.

6.1 Laser-induced grating spectroscopy

Mid-infrared LITGS has been applied for temperature measurements in laminar premixed CH_4/H_2/air and C_2H_4/air flat flames. Since water is one of the main products from combustion which has strong absorption in the mid-IR spectral region, the thermometry was based on water absorption at 3231 cm^{-1}. The robustness of the technique was investigated in product zone of CH_4/H_2/air flames with equivalence ratio ranging between $0.6 \leq \varphi \leq 1.05$, resulting in a single-shot temperature precision better than 1 % and an accuracy of 2.5 % of the flame temperature. The main uncertainty arises from the estimation of the gas composition in the probe volume, and thus the temperature calculation is affected by the values of the gas constants, γ/M_{gas}. The uncertainty in the LITGS-determined temperature was higher for the measurements performed in C_2H_4/air flames at fuel-rich conditions. It was observed that the gas constants varied significantly with the estimation of the H_2 concentration in the probe volume. Therefore, a thorough investigation considering the influence of H_2 needs to performed in future work.

The mid-IR LITGS excitation scan performed in the CH_4/H_2/air flame with φ=0.6 revealed the efficiency of thermalization for different ro-vibrational transitions of water, where some LITGS water lines appeared to have low or negligible intensity when compared to the corresponding absorption spectrum. This implies that a careful selection of the absorption line is needed in order to obtain strong LITGS signals. For future work, the energy transfer mechanism could be investigated in more detail, covering different ro-vibrational transitions.

The use of mid-IR pump laser beams in a LITGS setup provides the possibility of having large grating spacings (commonly between 30-60 μm), which produces signals of high quality with respect to the signal duration, intensity and number of oscillations. Common signal durations are around 1-5 μs. In LIGS experiments, the probe laser beam is aligned to intersect the laser-induced grating at the first Bragg angle. The larger grating spacings of mid-IR LITGS provided the possibility of aligning the probe laser beam in multiples of Bragg angle. However, these signals contained a multiple of the oscillation frequency, which is important to remember when using the oscillation frequency for calculations of speed of sound or temperature.

The probe volume of the mid-IR LITGS in this work was around $16\times0.5\times0.5$ mm^3 and it would be of interest to investigate the possibility to improve the spatial resolution using different alignment geometries where a good signal in terms of number of oscillation peaks, signal duration and intensity is obtained.

A potential application of O_2 LIGS for temperature measurements at 760 nm was investigated. At this wavelength the electrostrictive contribution to the LIGS signal was greater than the thermal contribution due to the smaller probe volume and higher pump laser energies compared to mid-IR LITGS. Temperature measurements up to 700 K resulted in detectable LIEGS signals using the alignment geometry presented in this work. However, at elevated pressures the thermalization process increased which resulted in distinguishable thermal and electrostrictive contributions in the resonant O_2 LITGS signals. The increase in pressure lead to longer signal durations due to the decrease in thermal diffusion, and high signal intensities due to increased reflectivity of the grating. The gained signal quality at elevated pressures suggest a useful application of O_2 LITGS for temperature measurements in high pressure fuel-lean flames. The presence of both an electrostrictive and thermal part to the LIGS signal at elevated pressures opens up the possibility of performing local concentration measurements, where the ratio between the oscillation peaks from electrostrictive and thermal acoustic wave contributions can be used.

The simulation model in this work was mainly employed to precisely extract the oscillation frequency, which was used in the temperature calculations. A future perspective would instead be to use the model in order to investigate the ro-vibrational energy transfer mechanism of the target molecular species in mid-IR.

Pump laser beams with duration of few nanoseconds are commonly used in a LIGS experiment. It would therefore be of interest to investigate the potential application of pump laser beams with short laser pulses on the picosecond or femtosecond scale, both in terms of resonant and non-resonant LIGS:

6.2 Degenerate four-wave mixing

Mid-IR DFWM has been applied for quantitative detection of hydrogen cyanide (HCN) released during gasification of straw pellets. The employment of an upconversion detector made it possible to perform sensitive measurements since it can provide up to 500 times better detection limit than the conventionally used InSb detector in the mid-IR region. Through a calibration process which considers the concentration and temperature dependence of the probed HCN absorption line, the intensity of the mid-IR DFWM signal could be converted to HCN concentration. The measurements were performed by tuning the laser wavelength to the peak of the HCN line since the process of HCN release from straw pellets is time-varying. The main uncertainty in the HCN concentration arises from the temperature measurements, which is based on obtaining the peak ratio between two groups of temperature sensitive hot water lines at 3230-3231.5 cm^{-1}. The temperature dependant peak ratio serves as a calibration for temperature and was in this work affected by the repeatability of positioning the laser line on the peak of the water lines. An alternative to the thermometry based on water line ratio would be mid-LITGS. As presented in this thesis, thermometry using mid-IR LITGS by probing hot water lines at 3231 cm^{-1} showed to be robust for applications in flames at atmospheric pressure. However, the determination of temperature relies on a good estimate of the gas composition in the probe volume. Therefore, a thorough investigation needs to be conducted if mid-IR LITGS can be applied for temperature measurements in biomass combustion, and especially during the devolatilization stage when numerous of different molecular species are released or formed.

Moreover, the feasibility of using mid-IR DFWM for detection of ammonia at 2.3 µm was investigated. These measurements indicated a limited performance in the detection limit due to the low absorption cross section of NH_3 in this spectral region. An improvement of the technique would be to use the upconversion detector equipped with a PPLN crystal designed for this wavelength region. In addition to that, ro-vibrational transitions in the fundamental vibrational band around 3 µm have higher absorption cross section and could be utilized. However, this band coincides with strong water absorption and a careful selection of the NH_3 absorption line needs to be made for applications in combusting environments.

The application of mid-IR DFWM in combination with the upconversion detector could be expanded for quantitative detection of other molecular species of interest during thermochemical conversion of biomass, such as hydrogen chloride (HCl) and different sulphur compounds. However, the quantitative detection relies on the selection of an absorption line that has a high absorption cross section and that it is free from interference from other species. The benefit of mid-IR laser beams is their less sensitivity to scattering from particles and could be applied in more particle-

laden environments where for example a number of pellets are combusted at the same time.

In terms of equipment, it would be beneficial to invest in a pressure cell which can be heated in order to use it as a tool for temperature and pressure investigations of both LIGS and DFWM signals. In addition to that, the described mid-IR laser system takes up most of the laboratory space and therefore it would be advantageous to construct a compact and mobile laser system setup, which can easily be applied and moved between different laboratories and measurement objects.

Bibliography

1. Kohse-Höinghaus, K., *Laser techniques for the quantitative detection of reactive intermediates in combustion systems*. Prog. Energy Combust. Sci., **20**(3): p. 203-279 (1994)

2. Aldén, M., Bood, J., Li, Z., and Richter, M., *Visualization and understanding of combustion processes using spatially and temporally resolved laser diagnostic techniques*. Proceedings of the Combustion Institute, **33**(1): p. 69-97 (2011)

3. Pender, J. and Hesselink, L., *Phase conjugation in a flame*. Optics Letters, **10**(6): p. 264-266 (1985)

4. Ewart, P. and O'Leary, S. V., *Detection of OH in a flame by degenerate four-wave mixing*. Optics Letters, **11**(5): p. 279-281 (1986)

5. Rahn, L. A. and Brown, M. S., *Polarization properties of degenerate four-wave mixing in flame OH*. Optics Letters, **19**(16): p. 1249-1251 (1994)

6. Williams, S., Rahn, L. A., Paul, P. H., Forsman, J. W., and Zare, R. N., *Laser-induced thermal grating effects in flames*. Optics Letters, **19**(21): p. 1681-1683 (1994)

7. Latzel, H., Dreizler, A., Dreier, T., Heinze, J., Dillmann, M., Stricker, W., Lloyd, G. M., and Ewart, P., *Thermal grating and broadband degenerate four-wave mixing spectroscopy of OH in high-pressure flames*. Applied Physics B, **67**(5): p. 667-673 (1998)

8. Boyd, R. W., *Nonlinear optics*, 3rd edition, Academic Press Inc., USA (2008)

9. Saleh, B. E. A. and Teich, M. C., *Fundamentals of Photonics*, 2nd edition, John Wiley & Sons, Hoboken, USA (2007)

10. Kiefer, J. and Ewart, P., *Laser diagnostics and minor species detection in combustion using resonant four-wave mixing*. Progress in Energy and Combustion Science, **37**(5): p. 525-564 (2011)

11. Kohse-Höinghaus, K. and Jefferies, J. B., *Applied combustion diagnostics*, Combustion: an international series, Taylor and Francis, New York, USA (2002)

12. Eckbreth, A. C., *Laser diagnostics for combustion temperature and species*, Combustion science and technology book series, 2nd edition, Gordon and Breach Science Publishers, Amsterdam, The Netherlands (1996)

13. Abrams, R. L. and Lind, R. C., *Degenerate four-wave mixing in absorbing media*. Optics Letters, **2**(4): p. 94-96 (1978)

14. Abrams, R. L. and Lind, R. C., *Degenerate four-wave mixing in absorbing media: errata*. Optics Letters, **3**(5) (1978)

15. Lucht, R. P., Farrow, R. L., and Rakestraw, D. J., *Saturation effects in gas-phase degenerate four-wave mixing spectroscopy: nonperturbative calculations*. Journal of the Optical Society of America B, **10**(9): p. 1508-1520 (1993)

16. Reichardt, T. A., Giancola, W. C., Shappert, C. M., and Lucht, R. P., *Experimental investigation of saturated degenerate four-wave mixing for quantitative concentration measurements*. Applied Optics, **38**(33): p. 6951-6961 (1999)

17. Bratfalean, R. T., Lloyd, G. M., and Ewart, P., *Degenerate four-wave mixing for arbitrary pump and probe intensities*. Journal of the Optical Society of America B, **16**(6): p. 952-960 (1999)

18. Reichardt, T. A. and Lucht, R. P., *Resonant degenerate four-wave mixing spectroscopy of transitions with degenerate energy levels: Saturation and polarization effects*. The Journal of Chemical Physics, **111**(22): p. 10008-10020 (1999)

19. Reichardt, T. and Lucht, R., *Effect of Doppler broadening on quantitative concentration measurements with degenerate four-wave mixing spectroscopy*. Journal of Optical Society of America B **13**(6): p. 1107-1119 (1996)

20. Reichardt, T. and Lucht, R., *Interaction of closely spaced resonances in degenerate four-wave-mixing spectroscopy*. Journal of Optical Society of America B **14**(10): p. 2449-2458 (1997)

21. Wandzura, S. M., *Effects of atomic motion on wavefront conjugation by resonantly enhanced degenerate four-wave mixing*. Optics Letters, **4**(7): p. 208-210 (1979)

22. Reichardt, T. A., Lucht, R. P., Danehy, P. M., and Farrow, R. L., *Theoretical investigation of the forward phase-matched geometry for degenerate four-wave mixing spectroscopy*. Journal of the Optical Society of America B, **15**(10): p. 2566-2572 (1998)

23. Bervas, H., Attal-Trétout, B., Labrunie, L., and Le Boiteux, S., *Four-wave mixing in OH: comparison between CARS and DFWM*. Il Nuovo Cimento D, **14**(10): p. 1043-1050 (1992)

24. Rakestraw, D. J., Farrow, R. L., and Dreier, T., *Two-dimensional imaging of OH in flames by degenerate four-wave mixing*. Optics Letters, **15**(12): p. 709-711 (1990)

25. Nyholm, K., *Two-dimensional imaging of OH in a flame by using degenerate four-wave mixing in a forward geometry*. Applied Physics B, **64**(6): p. 707-712 (1997)

26. Yip, B., Danehy, P. M., and Hanson, R. K., *Degenerate four-wave mixing temperature measurements in a flame*. Optics Letters, **17**(10): p. 751-753 (1992)

27. Lloyd, G. M., Hughes, I. G., Bratfalean, R., and Ewart, P., *Broadband Degenerate Four-Wave Mixing of OH for Flame Thermometry*. Appl. Phys. B: Lasers Opt., **67**(1): p. 107-113 (1998)

28. Ewart, P. and Kaczmarek, M., *Two-dimensional mapping of temperature in a flame by degenerate four-wave mixing in OH*. Applied Optics, **30**(27): p. 3996-3999 (1991)

29. Sun, Z. W., Li, Z. S., Li, B., and Aldén, M., *Flame temperature diagnostics with water lines using mid-infrared degenerate four-wave mixing*. Journal of Raman Spectroscopy, **42**(10): p. 1828-1835 (2011)

30. Voelkel, D., Chuzavkov, Y. L., Marquez, J., Orlov, S. N., Polivanov, Y. N., Smirnov, V. V., and Huisken, F., *Infrared degenerate four-wave mixing and resonance-enhanced stimulated Raman scattering in molecular gases and free jets*. Applied Physics B, **65**(1): p. 93-99 (1997)

31. Vander Wal, R. L., Holmes, B. E., Jeffries, J. B., Danehy, P. M., Farrow, R. L., and Rakestraw, D. J., *Detection of HF using infrared degenerate four-wave mixing*. Chemical Physics Letters, **191**(3): p. 251-258 (1992)

32. Sahlberg, A. L., Zhou, J., Aldén, M., and Li, Z. S., *Non-intrusive in situ detection of methyl chloride in hot gas flows using infrared degenerate four-wave mixing*. Journal of Raman Spectroscopy, **46**(8): p. 695-701 (2015)

33. Germann, G. J. and Rakestraw, D. J., *Multiplex Spectroscopy: Determining the Transition Moments and Absolute Concentrations of Molecular Species*. Science, **264**(5166): p. 1750 (1994)

34. Sun, Z. W., Li, Z. S., Li, B., Aldén, M., and Ewart, P., *Detection of C2H2 and HCl using mid-infrared degenerate four-wave mixing with stable beam alignment: towards practical in situ sensing of trace molecular species*. Applied Physics B, **98**(2): p. 593-600 (2010)

35. Germann, G. J., Farrow, R. L., and Rakestraw, D. J., *Infrared degenerate four-wave mixing spectroscopy of polyatomic molecules: CH4 and C2H2*. Journal of the Optical Society of America B, **12**(1): p. 25-32 (1995)

36. Sahlberg, A.-L., Zhou, J., Aldén, M., and Li, Z., *Investigation of ro-vibrational spectra of small hydrocarbons at elevated temperatures using infrared degenerate four-wave mixing*. Journal of Raman Spectroscopy, **47**(9): p. 1130-1139 (2016)

37. Tang, Y. and Reid, S. A., *Infrared degenerate four wave mixing spectroscopy of jet-cooled C2H2*. Chemical Physics Letters, **248**(5): p. 476-481 (1996)

38. Hot, D., Pedersen, R. L., Weng, W., Zhang, Y., Aldén, M., and Li, Z., *Spatially and temporally resolved IR-DFWM measurement of HCN released from gasification of biomass pellets*. Proceedings of the Combustion Institute, **37**(2): p. 1337-1344 (2019)

39. Sahlberg, A. L., Hot, D., Aldén, M., and Li, Z. S., *Non-intrusive, in situ detection of ammonia in hot gas flows with mid-infrared degenerate four-wave mixing at 2.3 μm*. Journal of Raman Spectroscopy, **47**(9): p. 1140-1148 (2016)

40. Farrow, R. L., Rakestraw, D. J., and Dreier, T., *Investigation of the dependence of degenerate four-wave mixing line intensities on transition dipole moment*. Journal of the Optical Society of America B, **9**(10): p. 1770-1777 (1992)

41. Danehy, P. M., Friedman-Hill, E. J., Lucht, R. P., and Farrow, R. L., *The effects of collisional quenching on degenerate four-wave mixing*. Applied Physics B, **57**(4): p. 243-248 (1993)

42. Bultitude, K., Bratfalean, R., and Ewart, P., *Saturation effects in molecular spectroscopy using degenerate four-wave mixing*. Journal of Raman Spectroscopy, **34**(12): p. 1030-1036 (2003)

43. Gordon, I. E., Rothman, L. S., Hill, C., Kochanov, R. V., Tan, Y., Bernath, P. F., Birk, M., Boudon, V., Campargue, A., Chance, K. V., Drouin, B. J., Flaud, J. M., Gamache, R. R., Hodges, J. T., Jacquemart, D., Perevalov, V. I., Perrin, A., Shine, K. P., Smith, M. A. H., Tennyson, J., Toon, G. C., Tran, H., Tyuterev, V. G., Barbe, A., Császár, A. G., Devi, V. M., Furtenbacher, T., Harrison, J. J., Hartmann, J. M., Jolly, A., Johnson, T. J., Karman, T., Kleiner, I., Kyuberis, A. A., Loos, J., Lyulin, O. M., Massie, S. T., Mikhailenko, S. N., Moazzen-Ahmadi, N., Müller, H. S. P., Naumenko, O. V., Nikitin, A. V., Polyansky, O. L., Rey, M., Rotger, M., Sharpe, S. W., Sung, K., Starikova, E., Tashkun, S. A., Auwera, J. V., Wagner, G., Wilzewski, J., Wcisło, P., Yu, S., and Zak, E. J., *The HITRAN2016 molecular spectroscopic database*. Journal of Quantitative Spectroscopy and Radiative Transfer, **203**: p. 3-69 (2017)

44. Rothman, L. S., Gordon, I. E., Barber, R. J., Dothe, H., Gamache, R. R., Goldman, A., Perevalov, V. I., Tashkun, S. A., and Tennyson, J., *HITEMP, the High-Temperature Molecular Spectroscopic Database*. J. Quant. Spectrosc. Radiat. Transfer, **111**(15): p. 2139-2150 (2010)

45. Stampanoni-Panariello, A., Hemmerling, B., and Hubschmid, W., *Temperature measurements in gases using laser-induced electrostrictive gratings*. Applied Physics B, **67**(1): p. 125-130 (1998)

46. Latzel, H., Dreizler, A., Dreier, T., Heinze, J., Dillmann, M., Stricker, W., Lloyd, G. M., and Ewart, P., *Thermal Grating and Broadband Degenerate Four-Wave Mixing Spectroscopy of OH in High-Pressure Flames*. Appl. Phys. B: Lasers Opt., **67**(5): p. 667-673 (1998)

47. Hayakawa, A., Yamagami, T., Takeuchi, K., Higuchi, Y., Kudo, T., Lowe, S., Gao, Y., Hochgreb, S., and Kobayashi, H., *Quantitative measurement of temperature in oxygen enriched CH4/O2/N2 premixed flames using Laser Induced Thermal Grating Spectroscopy (LITGS) up to 1.0 MPa*. Proceedings of the Combustion Institute, **37**(2): p. 1427-1434 (2019)

48. Luers, A., Sahlberg, A.-L., Hochgreb, S., and Ewart, P., *Flame thermometry using laser-induced-grating spectroscopy of nitric oxide*. Appl. Phys. B: Lasers Opt., **124**(3): p. 43 (2018)

49. Cummings, E. B., *Laser-Induced Thermal Acoustics: Simple Accurate Gas Measurements*. Opt. Lett., **19**(17): p. 1361-1363 (1994)

50. Cummings, E. B., Hornung, H. G., Brown, M. S., and DeBarber, P. A., *Measurement of gas-phase sound speed and thermal diffusivity over a broad pressure range using laser-induced thermal acoustics*. Optics Letters, **20**(14): p. 1577-1579 (1995)

51. Hart, R. C., Balla, R. J., and Herring, G. C., *Optical measurement of the speed of sound in air over the temperature range 300–650 K*. The Journal of the Acoustical Society of America, **108**(4): p. 1946-1948 (2000)

52. Eichler, H., Salje, G., and Stahl, H., *Thermal diffusion measurements using spatially periodic temperature distributions induced by laser light*. Journal of Applied Physics, **44**(12): p. 5383-5388 (1973)

53. Walker, D. J. W., Williams, R. B., and Ewart, P., *Thermal grating velocimetry*. Optics Letters, **23**(16): p. 1316-1318 (1998)

54. Kozlov, D. N., *Simultaneous characterization of flow velocity and temperature fields in a gas jet by use of electrostrictive laser-induced gratings*. Applied Physics B, **80**(3): p. 377-387 (2005)

55. Hemmerling, B., Kozlov, D. N., and Stampanoni-Panariello, A., *Temperature and flow-velocity measurements by use of laser-induced electrostrictive gratings*. Optics Letters, **25**(18): p. 1340-1342 (2000)

56. Stevens, R. and Ewart, P., *Single-shot measurement of temperature and pressure using laser-induced thermal gratings with a long probe pulse*. Applied Physics B, **78**(1): p. 111-117 (2004)

57. Hart, R. C., Herring, G. C., and Balla, R. J., *Pressure measurement in supersonic air flow by differential absorptive laser-induced thermal acoustics*. Optics Letters, **32**(12): p. 1689-1691 (2007)

58. Sahlberg, A.-L., Luers, A., Willman, C., Williams, B. A. O., and Ewart, P., *Pressure measurement in combusting and non-combusting gases using laser-induced grating spectroscopy*. Applied Physics B, **125**(3): p. 46 (2019)

59. Kiefer, J., Kozlov, D. N., Seeger, T., and Leipertz, A., *Local fuel concentration measurements for mixture formation diagnostics using diffraction by laser-induced gratings in comparison to spontaneous Raman scattering*. Journal of Raman Spectroscopy, **39**(6): p. 711-721 (2008)

60. Roshani, B., Flügel, A., Schmitz, I., Kozlov, D. N., Seeger, T., Zigan, L., Kiefer, J., and Leipertz, A., *Simultaneous measurements of fuel vapor concentration and temperature in a flash-boiling propane jet using laser-induced gratings*. Journal of Raman Spectroscopy, **44**(10): p. 1356-1362 (2013)

61. Hemmerling, B. and Kozlov, D. N., *Collisional relaxation of singlet O_2 in neat gas investigated by laser-induced grating technique*. Chem. Phys., **291**(3): p. 213-242 (2003)

62. Hubschmid, W., *Molecular relaxations in mixtures of O_2 with CO_2 observed on laser-induced gratings*. Appl. Phys. B: Lasers Opt., **94**(2): p. 345-353 (2009)

63. Hubschmid, W. and Hemmerling, B., *Relaxation processes in singlet O_2 analyzed by laser-induced gratings*. Chem. Phys., **259**(1): p. 109-120 (2000)

64. Kozlov, D. N., Kobtsev, V. D., Stel'makh, O. M., and Smirnov, V. V., *Study of Collisional Deactivation of $O_2(b^1\Sigma_g^+)$Molecules in a Hydrogen-Oxygen Mixture at High Temperatures using Laser-Induced Gratings*. J. Exp. Theor. Phys., **117**(1): p. 36-47 (2013)

65. Fantoni, R., Giorgi, M., De Dominicis, L., and Kozlov, D. N., *Collisional relaxation and internal energy redistribution in NO2 investigated by means of laser-induced thermal grating technique*. Chemical Physics Letters, **332**(3): p. 375-380 (2000)

66. Hemmerling, B. and Stampanoni-Panariello, A., *Imaging of flames and cold flows in air by diffraction from a laser-induced grating*. Applied Physics B, **57**(4): p. 281-285 (1993)

67. Förster, F. J., Crua, C., Davy, M., and Ewart, P., *Time-resolved gas thermometry by laser-induced grating spectroscopy with a high-repetition rate laser system*. Experiments in Fluids, **58**(7): p. 87 (2017)

68. De Domenico, F., Guiberti, T. F., Hochgreb, S., Roberts, W. L., and Magnotti, G., *Tracer-free laser-induced grating spectroscopy using a pulse burst laser at 100 kHz*. Optics Express, **27**(22): p. 31217-31224 (2019)

69. Willman, C. and Ewart, P., *Multipoint temperature measurements in gas flows using 1-D laser-induced grating scattering*. Experiments in Fluids, **57**(12): p. 191 (2016)

70. Sahlberg, A. L., Kiefer, J., Li, Z. S., and Aldén, M., *Mid-Infrared Pumped Laser-Induced Thermal Grating Spectroscopy for Detection of Acetylene in the Visible Spectral Range*. Applied Spectroscopy, **70**(6): p. 1034-1043 (2016)

71. Sahlberg, A.-L., Hot, D., Kiefer, J., Aldén, M., and Li, Z., *Mid-infrared laser-induced thermal grating spectroscopy in flames*. Proc. Combust. Inst., **36**: p. 4515-4523 (2017)

72. Kiefer, J., Sahlberg, A.-L., Hot, D., Aldén, M., and Li, Z., *Misalignment Effects in Laser-Induced Grating Experiments*. Applied Spectroscopy, **70**(12): p. 2025-2028 (2016)

73. Eichler, H. J., Günter, P., and Pohl, D. W., *Laser-induced dynamic gratings*, Springer Series in Optical Sciences, 1st edition, Springer-Verlag Berlin Heidelberg GmbH, New York, USA (1986)

74. Stampanoni-Panariello, A., Kozlov, D. N., Radi, P. P., and Hemmerling, B., *Gas Phase Diagnostics by Laser-Induced Gratings I. Theory*. Appl. Phys. B: Lasers Opt., **81**(1): p. 101-111 (2005)

75. Cummings, E. B., Leyva, I. A., and Hornung, H. G., *Laser-Induced Thermal Acoustics (LITA) Signals from Finite Beams*. Appl. Opt., **34**(18): p. 3290-3302 (1995)

76. Paul, P. H., Farrow, R. L., and Danehy, P. M., *Gas-Phase Thermal-Grating Contributions to Four-Wave Mixing*. J. Opt. Soc. Am. B., **12**(3): p. 384-392 (1995)

77. Stampanoni-Panariello, A., Kozlov, D. N., Radi, P. P., and Hemmerling, B., *Gas-phase diagnostics by laser-induced gratings II. Experiments*. Applied Physics B, **81**(1): p. 113-129 (2005)

78. Hemmerling, B., Hubschmid, W., Kozlov, D. N., and Stampanoni, A. *Diagnostics in gases by transient laser-induced electrostrictive gratings*. 1999.

79. Latzel, H. and Dreier, T., *Sound velocity, heat conduction and virial coefficients of gaseous mixtures at high pressure from NIR laser-induced grating experiments*. Physical Chemistry Chemical Physics - PHYS CHEM CHEM PHYS, **2**: p. 3819-3824 (2000)

80. Hubschmid, W., Bombach, R., Hemmerling, B., and Stampanoni-Panariello, A., *Sound-velocity measurements in gases by laser-induced electrostrictive gratings*. Applied Physics B, **62**(1): p. 103-107 (1996)

81. NIST, *REFPROP*. 2020; Available from: https://www.nist.gov/srd/refprop.

82. Stampanoni-Panariello, A., Hemmerling, B., and Hubschmid, W., *Temperature measurements in gases using laser-induced electrostrictive gratings*. Appl. Phys. B: Lasers Opt., **67**(1): p. 125-130 (1998)

83. Stampanoni-Panariello, A., Hemmerling, B., and Hubschmid, W., *Electrostrictive generation of nonresonant gratings in the gas phase by multimode lasers*. Physical Review A, **51**(1): p. 655-662 (1995)

84. Kozlov, D. N., Kiefer, J., Seeger, T., Fröba, A. P., and Leipertz, A., *Simultaneous Measurement of Speed of Sound, Thermal Diffusivity, and Bulk*

Viscosity of 1-Ethyl-3-Methylimidazolium-Based Ionic Liquids Using Laser-Induced Gratings. J. Phys. Chem. B., **118**: p. 14493-14501 (2014)

85. Hubschmid, W., Hemmerling, B., and Stampanoni-Panariello, A., *Rayleigh and Brillouin modes in electrostrictive gratings*. J. Opt. Soc. Am. B, **12**(10): p. 1850-1854 (1995)

86. Hemmerling, B., Kozlov, D. N., Stel'makh, O. M., and Attal-Trétout, B., *Diagnostics of water-containing gas mixtures using thermal laser-induced gratings*. Chemical Physics, **320**(2): p. 103-117 (2006)

87. Li, Z. S., Rupinski, M., Zetterberg, J., Alwahabi, Z. T., and Aldén, M., *Mid-infrared polarization spectroscopy of polyatomic molecules: Detection of nascent CO2 and H2O in atmospheric pressure flames*. Chemical Physics Letters, **407**(4): p. 243-248 (2005)

88. Thorlabs, *Optical substrates*. 2020; Available from: https://www.thorlabs.com.

89. Dam, J. S., Tidemand-Lichtenberg, P., and Pedersen, C., *Room-temperature mid-infrared single-photon spectral imaging*. Nature Photonics, **6**: p. 788 (2012)

90. Høgstedt, L., Dam, J. S., Sahlberg, A.-L., Li, Z., Aldén, M., Pedersen, C., and Tidemand-Lichtenberg, P., *Low-noise mid-IR upconversion detector for improved IR-degenerate four-wave mixing gas sensing*. Optics Letters, **39**(18): p. 5321-5324 (2014)

91. Pedersen, R. L., Hot, D., and Li, Z., *Comparison between a InSb Detector and Upconversion Detector for Infrared Polarization Spectroscopy*. Applied Spectroscopy **72**(5): p. 793-797 (2018)

92. Pedersen, R. L., *Upconversion Detection for Improved Nonlinear Mid-infrared Spectroscopy in Flames.* Department of Physics, Lund University, Lund (2019)

93. Pedersen, R. L. and Li, Z., *Infrared Degenerate Four-wave Mixing with Upconversion Detection for Quantitative Gas Sensing*. JoVE, (145): p. e59040 (2019)

94. Weng, W., Borggren, J., Li, B., Aldén, M., and Li, Z., *A novel multi-jet burner for hot flue gases of wide range of temperatures and compositions for optical diagnostics of solid fuels gasification/combustion*. Review of Scientific Instruments, **88**(4): p. 045104 (2017)

95. Weng, W., *Optical Diagnostics for Quantitative Potassium Chemistry in Biomass Thermochemical Conversion Processes.* Department of Physics, Lund University, Lund (2020)

96. Herzberg, L. and Herzberg, G., *Fine Structure of the Infrared Atmospheric Oxygen Bands*. The Astrophysical Journal, **105**: p. 353 (1947)

97. Babcock, H. D. and Herzberg, L., *Fine Structure of the Red System of Atmospheric Oxygen Bands*. The Astrophysical Journal, **108**: p. 167 (1948)

98. Brown, L. R. and Plymate, C., *Experimental Line Parameters of the Oxygen A Band at 760 nm*. Journal of Molecular Spectroscopy, **199**(2): p. 166-179 (2000)

99. De Domenico, F., Guiberti, T. F., Hochgreb, S., Roberts, W. L., and Magnotti, G., *Temperature and water measurements in flames using 1064 nm Laser-Induced Grating Spectroscopy (LIGS)*. Combustion and Flame, **205**: p. 336-344 (2019)

100. Gordon, S. and McBride, B. J., *NASA Reference Publication 1311: Computer Program for Calculation of Complex Chemical Equilibrium Compositions and Applications*. 1996: National Aeronautics and Space Administration.

101. Kearney, S. P., *Hybrid fs/ps rotational CARS temperature and oxygen measurements in the product gases of canonical flat flames*. Combustion and Flame, **162**(5): p. 1748-1758 (2015)

102. Miller, J. D., Slipchenko, M. N., Meyer, T. R., Stauffer, H. U., and Gord, J. R., *Hybrid femtosecond/picosecond coherent anti-Stokes Raman scattering for high-speed gas-phase thermometry*. Optics Letters, **35**(14): p. 2430-2432 (2010)

103. Richardson, D. R., Lucht, R. P., Kulatilaka, W. D., Roy, S., and Gord, J. R., *Theoretical modeling of single-laser-shot, chirped-probe-pulse femtosecond coherent anti-Stokes Raman scattering thermometry*. Applied Physics B, **104**(3): p. 699 (2011)

104. Brown, M. S. and Roberts, W. L., *Single-Point Thermometry in High-Pressure, Sooting, Premixed Combustion Environments*. Journal of Propulsion and Power, **15**(1): p. 119-127 (1999)

105. Stevens, R. E., *Laser-induced grating techniques for combustion diagnostics.* University of Oxford, Oxford (2004)

106. Leppälahti, J. and Koljonen, T., *Nitrogen evolution from coal, peat and wood during gasification: Literature review*. Fuel Processing Technology, **43**(1): p. 1-45 (1995)

107. Glarborg, P., Jensen, A. D., and Johnsson, J. E., *Fuel nitrogen conversion in solid fuel fired systems*. Progress in Energy and Combustion Science, **29**(2): p. 89-113 (2003)

108. Ren, Q. and Zhao, C., *Evolution of fuel-N in gas phase during biomass pyrolysis*. Renewable and Sustainable Energy Reviews, **50**(Supplement C): p. 408-418 (2015)

109. Chen, Z., Yuan, S., Liang, Q., Wang, F., and Yu, Z., *Distribution of HCN, NH3, NO and N2 in an entrained flow gasifier*. Chemical Engineering Journal, **148**(2): p. 312-318 (2009)

110. Rothman, L. S., Gordon, I. E., Babikov, Y., Barbe, A., Chris Benner, D., Bernath, P. F., Birk, M., Bizzocchi, L., Boudon, V., Brown, L. R., Campargue, A., Chance, K., Cohen, E. A., Coudert, L. H., Devi, V. M., Drouin, B. J., Fayt, A., Flaud, J. M., Gamache, R. R., Harrison, J. J., Hartmann, J. M., Hill, C., Hodges, J. T., Jacquemart, D., Jolly, A., Lamouroux, J., Le Roy, R. J., Li, G., Long, D. A., Lyulin, O. M., Mackie, C. J., Massie, S. T., Mikhailenko, S., Müller, H. S. P., Naumenko, O. V., Nikitin, A. V., Orphal, J., Perevalov, V., Perrin, A., Polovtseva, E. R., Richard, C., Smith, M. A. H., Starikova, E., Sung, K., Tashkun, S., Tennyson, J., Toon, G. C., Tyuterev, V. G., and Wagner, G., *The HITRAN2012 molecular spectroscopic database*. Journal of Quantitative Spectroscopy and Radiative Transfer, **130**: p. 4-50 (2013)

Acknowledgements

All work presented in this thesis has been performed at the Division of Combustion Physics at Lund University and during my years here I have met and worked with many inspiring people who have made this thesis possible.

First, I would like to thank my supervisors *Zhongshan Li* and *Marcus Aldén* for giving me the opportunity to pursue a PhD degree at the division of Combustion Physics and for your support and help along this journey. I appreciate your encouragement to keep looking for absorption lines or applying the techniques in more realistic environments. A special thanks to *Zhongshan Li* for sharing many research ideas that challenged me to think outside the box and for letting me find my own path in the lab.

‹No man is an island› is especially true when it comes to doing research. I would like to acknowledge all of my co-workers who were involved in the different projects. Thanks to *Anna-Lena Sahlberg* for being a great co-worker and sharing the excitement when getting a signal in the lab. I want to thank *Rasmus L. Pedersen* for many creative optical solutions and for being a joy to work with. Thanks to *Wubin Weng* for sharing your broad knowledge about biomass combustion and to *Kajsa Larsson* for your tireless efforts when we were aligning the KrF excimer laser in the ozone projects. Thanks also to *Johannes Kiefer* for introducing us to LITGS and for the incredibly efficient measurement campaigns. Thanks to *Maria Ruchkina*, *Pengji Ding* and *Joakim Bood* for the exciting cooperation during the femtosecond LIGS project. I look forward to see where it leads.

During my time at the division I had the privilege to share office first with *Zheming Li* and later with *Pengji Ding*. I would like to thank both of you for introducing me to combustion engines and backward lasing, and for all discussions that required the use of a whiteboard.

I want to thank *Sven-Inge Möller* for your uplifting discussions and support during these years and *Per-Erik Bengtsson* for giving me the opportunity to supervise the lab Förbränning för F2.

I am grateful to *Minna Ramkull* and *Cecilia Bille* for all the help throughout the years and for bringing art and economical aspects to my research. Thanks also to

Igor Buzuk and *Rutger Lorensson* for providing smart solutions to my electronic and mechanical problems in the lab.

I want to thank *everyone* at the division who has shared equipment with me for various research and teaching activities.

A special thanks to *Panagiota Stamatoglou* and *Sandra Török*, I could not have asked for better companions during this journey and I am grateful that we made it together. I also want to acknowledge *Arman Subash* for putting everything in perspective and being a good friend, *Alexios Matamis*, for your deep technical analysis and motivating me to buy a real car (while there is still a chance!) and *Jim Larsson* for sharing the enthusiasm for absorption spectroscopy and reminding me to take breaks now and then. I would also like to thank *Yupan Bao* for sharing your enthusiasm about fast cars, *Thi Kim Cuong Le* for your encouragement, *Saeed Derafshzan*, *Manu Mannazhi* and *Haisol Kim* for the memorable glacier hike during GRC. Thanks also to present and past colleagues, *Eduoard Berrocal*, *Yogeshwar Nath Mishra*, *Marco Lubrano Lavadera*, *Xin Liu*, *Meng Li*, *Shen Li*, *Jinlong Gao*, *Jianfeng Zhou*, *Moah Christensen* and *Fahed Abou Nada* for providing help and support in various ways.

I want to thank the members of the Combustion Climbing group for always challenging me to reach new heights!

Apart from my research activities I got the opportunity to work with *Isabel Gallardo González* and *Egle Bukarte* on the female researcher network at Lund Laser Centre. Thank you both for being a source of inspiration and for all early morning meetings!

I would like to acknowledge the organizations and foundations that made this research possible; European Research Council (ERC) through the advanced grant TUCLA, Swedish Energy Agency (Energimyndigheten) through Centre of Combustion Science and Technology (CECOST) and Knut & Alice Wallenberg foundation.

Finally, I would like to thank my family and friends for your constant encouragement and ever-present support throughout these years.

May the m·a be with you!